

The Global Kinematics of the Globular Cluster M15

G.A. Drukier, S.D. Slavin, H.N. Cohn, P.M. Lugger, and R.C. Berrington
Department of Astronomy, Indiana University, Bloomington, Indiana

B.W. Murphy

Department of Physics and Astronomy, Butler University, Indianapolis, Indiana

and

P.O. Seitzer

Department of Astronomy, University of Michigan, Ann Arbor, Michigan

ABSTRACT

We present velocities for 230 stars in the outer parts of the globular cluster M15 measured with the Hydra multi-object spectrograph on the WIYN telescope. A new Bayesian technique is used for analyzing the data. The mean velocity of the cluster is $-106.9 \pm 0.3 \text{ km s}^{-1}$. Rotation with an amplitude of $1.5 \pm 0.4 \text{ km s}^{-1}$ and a position angle of $125 \pm 19^\circ$ is observed and the model including rotation is marginally favored over one without rotation. The velocity dispersion decreases from the center out to about $7'$ and then appears to increase slightly. This behavior is strikingly different from the continued decline of velocity dispersion with increasing radius that is expected in an isolated cluster. We interpret this as an indication of heating of the outer part of M15 by the Galactic tidal field.¹

Subject headings: globular clusters: individual (M15) — methods: statistical

1. Introduction

1.1. Theoretical Background

A full understanding of globular cluster dynamical evolution—including the core-collapse process and its aftermath—requires that global dynamical models be fit to global data sets. In

¹Table 2 in this paper contains the velocities of the 230 stars deemed to be members of the cluster. A table of 361 stars with velocities which are non-members will not be published, this table and Table 2 are both available electronically from the Astronomical Data Center (ADC). The ADC's Internet site hosts WWW and FTP access to the ADC's archives at the URL <http://adc.gsfc.nasa.gov/>

close analogy with the strong coupling between a stellar core and envelope, there is a strong interaction between the core and halo of a globular cluster. For both stars and clusters, the energy-transport rate in the outer parts determines the time-averaged rate of energy generation in the core (Hut et al. 1992). In clusters, star-star gravitational scattering is the energy-transport mechanism and hard binaries are the central energy source.

Over the past few years, we have fit isotropic Fokker-Planck models to the surface density and velocity dispersion profiles of several collapsed-core clusters including M15 (Grabhorn et al. 1992, Dull et al. 1997), NGC 6624 (Grabhorn et al. 1992), and NGC 6397 (Drukier 1995). We have recently extended our Fokker-Planck approach to the accurate treatment of an anisotropic velocity distribution (Drukier et al. 1997). This will allow us to produce fully global models that include the radial-orbit bias that develops in cluster halos. Fitting dynamical models depends crucially on the availability of kinematic data, since surface-brightness or star-count profiles alone do not strongly constrain such important parameters as the mass-function slope or the total cluster mass.

In addition to evolving as a result of internal energy transport, clusters also respond to external tidal perturbations resulting from interactions with the Galaxy. Such perturbations include shocks caused by the cluster’s passage by the bulge or through the disk, and a steady tidal acceleration from the smoother halo potential. In both cases, there is energy input to the cluster, producing a “heating” effect, although the latter is usually treated as a boundary condition causing the clusters to lose mass. While primarily the energy is directly deposited in the outer part of the cluster’s mass distribution, as was first demonstrated by Spitzer and Chevalier (1973) the evolution of the entire cluster is affected. In particular, they found that tidal shocking tends to accelerate core collapse.

The extent of tidal heating and its effect on the evolution of a cluster has been of continuing theoretical interest. A particular motivation is that tidal heating appears to be a major contributing factor to the destruction of globular clusters (Aguilar, Hut, & Ostriker 1988; Okazaki & Tosa 1995; Capriotti & Hawley 1996; Gnedin & Ostriker 1997). Kundić & Ostriker (1995) have given the most recent theoretical analysis of the expected heating of globular clusters by tidal shocks. They have shown that the second-order, tidal-shock relaxation term, neglected in many previous studies, is usually more important than the first-order term, both for the impulse and adiabatic approximations. Weinberg (1994) demonstrated that the usual adiabatic approximation does not apply in a three-dimensional potential, and this has been included in the analysis of Kundić & Ostriker (1995). From their analysis, it appears that tidal effects are locally important as far into a cluster as the half-mass radius.

Of particular relevance for comparison with the observations of the global velocity dispersion profile of M15 presented here, are models for cluster evolution that include tidal effects. What are needed are numerical predictions to compare with our velocity distribution observations. Unfortunately, most papers dealing with this have failed to provide an analysis that may be

directly compared with the usual velocity dispersion profile determinations. One exception is Allen & Richstone (1988). This study, which only looked at the first-order effect, found that the velocity dispersion increases for the escaping stars found in the outermost part of a cluster. They determined the tidal radius by the minimum in the velocity dispersion profile. This tidal radius and the difference between the radial and tangential velocity dispersion profiles depended on the nature of the assumed cluster orbit. Oh & Lin (1992) present a hybrid approach, which uses a Fokker-Planck approach for treating internal relaxation (using the second order Fokker-Planck terms only) and direct orbit integration for including the effects of the tidal field. However, they do not provide results for the evolution of the velocity dispersion profile.

1.2. Observational Background

As the prototypical collapsed-core globular cluster, M15 has received considerable observational attention. Recent Hubble Space Telescope (HST) imaging studies have probed the stellar distribution in the central region with increasingly higher angular resolution (Lauer et al. 1991, De Marchi & Paresce 1994, 1995, Guhathakurta et al. 1996, Sosin & King 1997). The current consensus of this work is that the surface density profile of M15 has a central power-law form, with no clear evidence for a resolved core. The tightest upper limit on the core radius is $1''.5$ (Sosin & King 1997). These results have been combined with ground-based surface brightness measurements (Lugger et al. 1995) and star counts (King et al. 1968) to generate a global surface density profile for Fokker-Planck model fits (Dull et al. 1997). The structure of the outermost region of M15 has recently been studied by Grillmair et al. (1995). They carried out two-color stellar photometry using digitized Schmidt plates and used the color-magnitude diagram to statistically correct for foreground contamination, thus allowing them to map out the large-radius density profile of the cluster. They found an apparent tidal radius of $23'$ for M15, based on a King (1966) model fit. They also found an excess population of cluster stars beyond this radius, which they interpreted as a tidal tail.

A number of studies have been carried out over the past decade to determine the velocity dispersion profile of M15 (Peterson, Seitzer, & Cudworth 1989; Gebhardt et al. 1994, 1997; Dull et al. 1997). These studies have all concentrated on the central region of the cluster. The greatest radial offset for any star in the Peterson et al. (1989) sample is $4'.6$; the other studies surveyed the central $1 - 2'$ radius about the cluster center. Peterson et al. (1989) and Dull et al. (1997) used long slit spectroscopy, while Gebhardt et al. (1994, 1997) used Fabry-Perot imaging spectrophotometry to scan the $H\alpha$ line.

The key finding by Peterson et al. (1989) is that the velocity dispersion profile of M15 rises rapidly towards the cluster center. While subsequent studies by Gebhardt et al. (1994, 1997) and Dull et al. (1997) confirm the rising nature of the profile within the central arc minute,

these recent studies plus that of Dubath, Meylan & Mayor (1994) obtained a central velocity dispersions between 11 and 14 km s^{-1} , much less than the 25 km s^{-1} found by Peterson et al. (1989). As discussed by Dull et al. (1997), the global surface density profile of M15 and the velocity dispersion profile out to about 4' is well fitted by a Fokker-Planck model that contains a substantial, centrally concentrated population of non-luminous remnants — presumably neutron stars. Multi-mass, King-type models do not provide as good a joint fit to the surface-density and velocity-dispersion profiles (Dull et al. 1997; Sosin & King 1997).

In this study, we present the first velocity information for the outermost region of M15. The 230 cluster members identified in our sample primarily lie in the range of 1 – 16'6 from the cluster center. Thus, our work complements that of Gebhardt et al. (1997), who have presented velocities for 1534 stars that primarily lie within 1'5 of the cluster center. Our median velocity accuracy is 0.3 km s^{-1} ; the velocity accuracies for the Gebhardt et al. (1997) sample vary over a range of 0.5 – 10 km s^{-1} .

The following section describes our observations and presents our velocity measurements. Our analysis technique, which is new for this application, uses Bayesian statistical methods. These are described in §3. Section 4 gives our analysis of the velocities of the members. In the final section, we interpret our results in the context of models for clusters evolving under the influence of tidal effects.

2. The Data

2.1. Observations

All of the new observations discussed here were obtained using the Hydra multi-fiber spectrograph on the 3.5m WIYN telescope.² This instrument has 100 fibers which can each be placed within the 1° diameter observing field to 0'2 precision. The minimum fiber separation is 36'', so while the central 0'5 of the cluster cannot be efficiently observed, this instrument is ideal for observing the outer region of globular clusters. We were able to observe up to 80 stars at a time. For all observations we used the echelle grating with an order centered at 515 nm, in the neighborhood of the Mg b lines. Approximately 20nm of the order was imaged on the 2048 pixel long CCD for a dispersion of about 0.01 nm/pixel. The comparison source was a Th-Ar lamp.

Use of Hydra requires accurate positions for the stars to be observed. The positions of the stars came from two sources, a 3 × 3 mosaic of Curtis-Schmidt frames in *V* and *I* and a list from K. Cudworth of the stars on his M15 proper motion program. This list filled in the center of the

²The WIYN Observatory is a joint facility of the University of Wisconsin, Indiana University, Yale University, and the National Optical Astronomy Observatories.

cluster which was too crowded on the Schmidt frames to allow accurate photometry. The positions of the stars were reduced to the astrometric system of the *HST Guide Star Catalogue* and proved, at the telescope, to be very reliable.

The input list contained over 13,000 stars, the bulk of which are non-members. Given our choice of spectral region, we restricted our observations to stars on the giant branch. Our candidates were therefore selected to lie in this region of the V vs. $(V - I)$ color-magnitude diagram. We observed M15 during the course of three observing runs, one each in May, June, and October 1996. Table 1 contains a log of the observations. The May 1996 run was in a sense experimental and took place before the full input list was produced. We only had astrometry from the central Schmidt frame as well as the positions of Cudworth’s stars. Because of the restricted region of candidates we could only observe of order 25 stars per Hydra set up. In June 1996 the full list was available and we observed virtually all the stars on the giant branch brighter than $V = 15.7$ and outside about $4'$. In October 1996 we re-observed all the known members between $4'$ and $18'$, some of the central stars, and an additional sample on the giant branch with $15.7 < V < 16.6$ and $4' < r < 17'$. As the October run progressed we did rough reductions of the spectra to weed out non-members and to get additional spectra of apparent members. Figure 1 shows the distribution of observed stars in radius and magnitude. The diagram is a version of a ‘sunflower’ plot (Cleveland & McGill 1984). The number of points on each symbol represents the number of observations with the stars represented by small circles being observed once and those by diagonal lines twice. We obtained, in total, 1132 spectra of 591 stars in the M15 field. Of these, 230 turned out to be members. Membership was determined by velocity coherence and the strength of the absorption lines as will be discussed further below.

At least one of the stars K144 and K1040 were observed in each Hydra configuration (a ‘setup’). The former proved to have a variable radial velocity which changed by 1 km s^{-1} between May and June and 1.4 km s^{-1} between June and October. The velocities for K1040 were much more consistent and its spectrum was used as the template for the velocity determination by cross-correlation.

2.2. Spectral Reduction

The data were reduced using the *dohydra* reduction package in IRAF³. Each observation was accompanied by one or more 5-minute exposures of an incandescent lamp (a ‘flat’) taken with the fibers in the same configuration as the observations. Generally, setups observed at the ends of the night had multiple flat exposures, but, due to the overhead involved with flats and especially

³IRAF is distributed by the National Optical Astronomy Observatories, which are operated by the Association of Universities for Research in Astronomy, Inc., under cooperative agreement with the National Science Foundation.

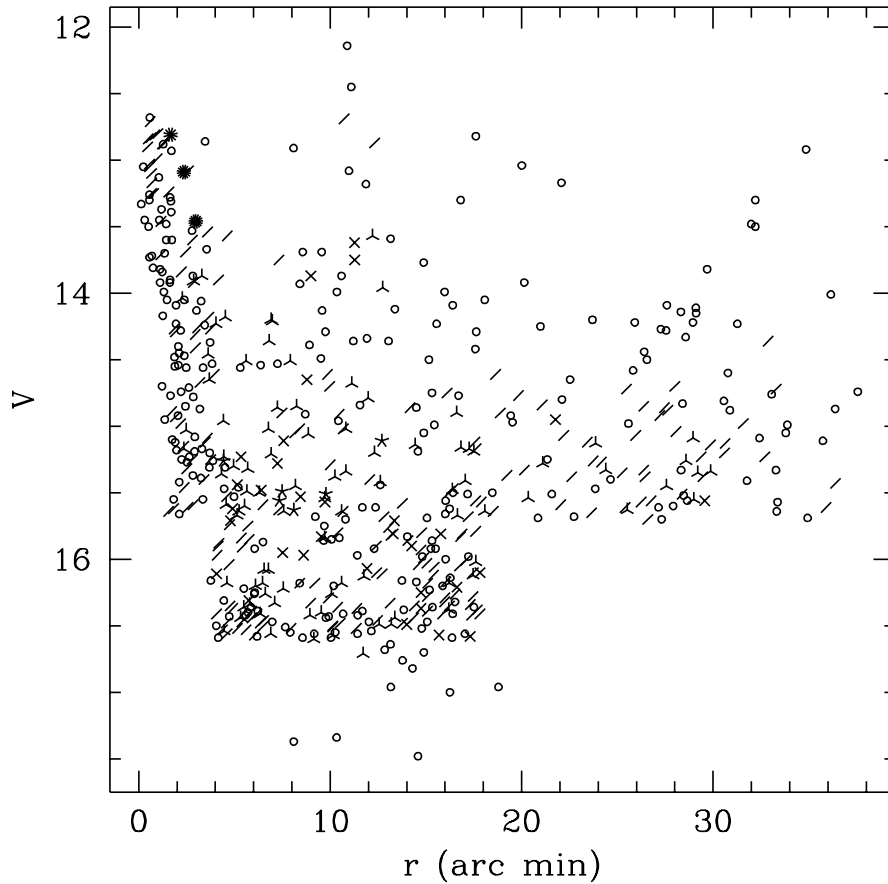


Fig. 1.— Distribution of observed stars in radial position and V magnitude. The number of points on each symbol represents the number of observations. A small circle represents a single observation and a diagonal line two.

with reconfiguring the fibers, usually single flat exposures were done. There did not appear to be any disadvantage to using single exposures since cosmic rays were not a great problem. The program exposures and bracketing Th-Ar lamp exposures were extracted and then divided by the extracted lamps. No sky subtraction was required owing to the high-dispersion and the absence of the moon; all observations were taken in dark time. The wavelength calibration was done using 36 comparison lines. The fifth-order dispersion solution generally had RMS residuals of less than 10^{-4} nm or 0.05 km s $^{-1}$. During dispersion correction the spectra were re-sampled into 2048 logarithmically spaced bins covering 20.7 nm in total.

Cosmic ray removal was done through the simple expedient of using the IRAF *continuum* task to replace with the continuum fit all pixels more than 4 standard deviations above the fit or 9 standard deviations below the fit. The latter was necessary due to the re-sampling of the

spectra during dispersion correction. The spline interpolation required for re-sampling sometimes gave complimentary negative spikes around large cosmic rays. Care was taken not to remove any genuine absorption lines. Some artificial lines, arising in re-sampling but falling under the nine-standard-deviation limit, may have been added, but this would not have had a large effect on the resulting velocities given the large number of real lines dominating the cross-correlation.

In 1996 May and October, multiple exposures were taken with each fiber configuration. The resulting spectra were added together to produce the final spectra for cross-correlation. The four exposures in the October ‘Q’ configuration were taken on two consecutive nights due to clouds, but were nevertheless combined, since the faintest stars lacked adequate flux in either pair. These were first shifted by a velocity equivalent to the difference in the Earth’s heliocentric velocity relative to M15 between the two observations.

2.3. Cross-correlation, the Velocity Uncertainties, and the Zero point

There were 33 individual exposures of K1040, totaling over 22 hours of exposure time. These were shifted to remove small differences in the geocentric velocity and were summed to form the high signal-to-noise template shown in Figure 2. The stellar velocities were measured relative to this template using the cross-correlation technique of Tonry & Davis (1979) encoded in the IRAF *fxcor* task. This computes the cross-correlation function of the Fourier transforms of the template and stellar spectra. The shift of the cross-correlation peak from zero gives the velocity of the program star relative to the template. This was computed for all the extracted stellar spectra. We excluded from further analysis all spectra with cross-correlation peaks less than 0.2. These spectra had low signal-to-noise ratios and the velocities derived were often obviously due to the selection of chance peaks in the cross-correlations, since they often gave velocities of several 1000 km s⁻¹.

The uncertainties in the velocities, ϵ_v , were determined from the ratio, R , of the peak of the cross-correlation function to the size of the random noise fluctuations. For each spectrum $\epsilon_v = C/(1 + R)$ (Tonry & Davis 1979). The constant C depends on the number of resolution elements in the observation and on the width of the cross-correlation function. In practice the value of C is established from the data. We have used the procedure of Pryor, Latham & Hazen (1988) to calculate C . For all stars observed more than once in an observing run we have computed the statistic

$$\epsilon = \frac{\Delta v}{\left((1 + R_1)^{-2} + (1 + R_2)^{-2} \right)^{\frac{1}{2}}}. \quad (1)$$

After weeding out possible variables we have 228 pairs of repeat observations. Using the Bayesian procedure described in Section 3, we have calculated the dispersion of the distribution of ϵ assuming a zero mean. This gives $C = 13.1 \pm 0.5$ km s⁻¹, which is the value used in computing the errors in the velocity tables.

The velocity zero point was established using six, high signal-to-noise exposures of the

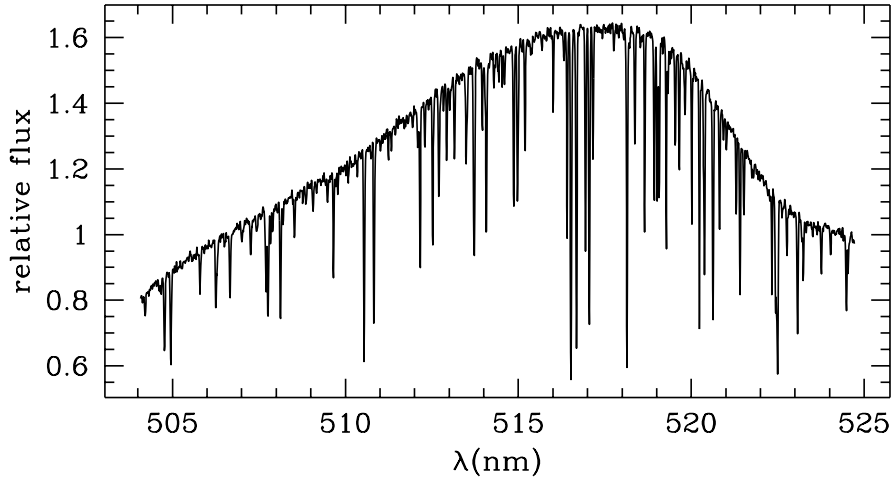


Fig. 2.— Template spectrum used for cross-correlations. This is a combination of 33 individual spectra of K1040 adjusted for heliocentric velocity differences.

twilight sky, two taken in 1996 May and four in 1996 October. The fibers in these exposures had various configurations. The spectra in these exposures were extracted and wavelength-calibrated in the usual way and these individual spectra were cross-correlated against the K1040 template spectrum. The average velocity for the spectra in each sky exposure was calculated. The internal dispersions were between 0.10 and 0.24 km s^{-1} , and the mean error in a single velocity was 0.6 km s^{-1} using $C = 13.1 \text{ km s}^{-1}$ as above. The difference between the internal dispersion and the individual uncertainties might suggest that the individual errors are overestimated. On the other hand, the standard deviation of the six mean velocities about their mean is 0.5 km s^{-1} which is quite consistent with the error estimate. What this indicates is that while the velocities of the spectra in an exposure can be measured consistently, there are systematic differences between exposures as well. Since there is agreement between the standard deviation of the velocities in the six exposures and the errors of the individual velocities, we can have some confidence that our value for C and hence for the uncertainties are correct. This is important for the subsequent calculation of the cluster velocity dispersion. The zero point is taken as the unweighted mean of the six mean velocities and is $-99.4 \pm 0.2 \text{ km s}^{-1}$. The velocity of K1040 itself is derived in the same way as for the rest of the stars. Its mean velocity with respect to the template is $0.04 \pm 0.03 \text{ km s}^{-1}$.

As a final check we compare our velocities against the velocities of stars in common with those observed by Peterson et al. (1989) and Gebhardt et al. (1997). Figures 3 and 4 compare the velocities of the common stars. There are 79 stars in common between our data and Peterson et al. (1989) and 42 between our data and Gebhardt et al. (1997), where we have only included the new velocities reported by Gebhardt et al. The outlying star in Fig. 3 is K673 which is claimed

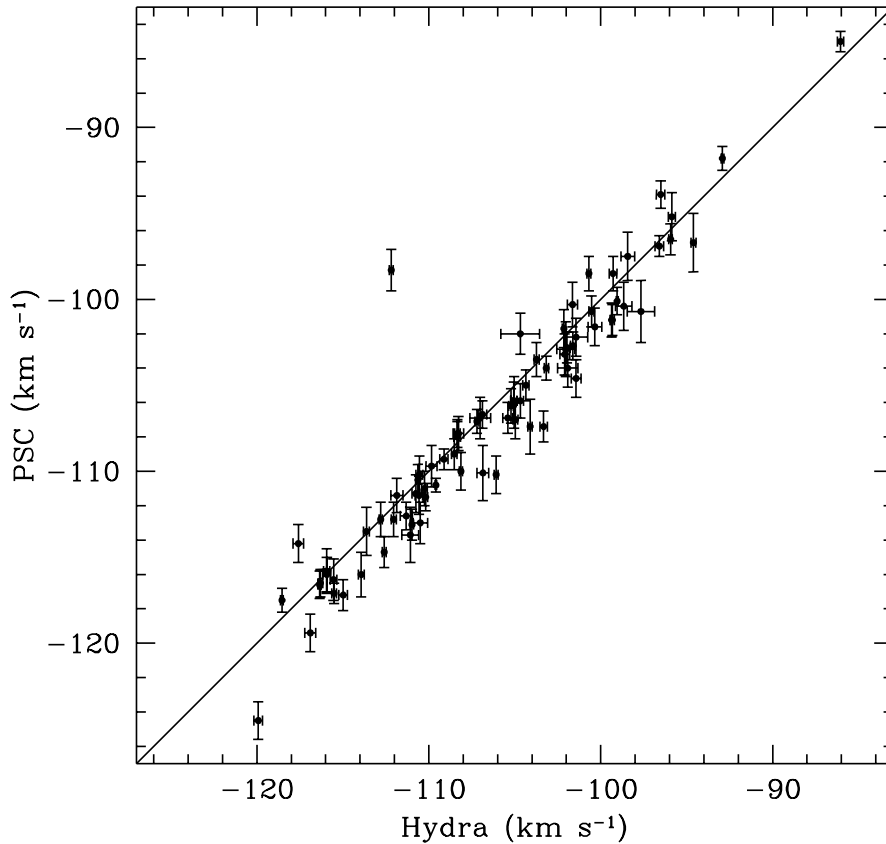


Fig. 3.— Comparison of our velocities with those of Peterson et al. (1989). The star with a large deviation is K673, a probable variable.

by Gebhardt et al. (1994) to be a binary. The Peterson et al. velocity is the most discrepant. Most of the stars in Fig. 4 lying off of the equality line are noted as being variable in one or other of our studies. For four of the Gebhardt et al. variables, we also have multiple observations and we confirm three of them. One further possible variable is not confirmed. The apparent zero-point shift is not statistically significant for the full sample, but, for the non-variables, there is a correlation between declination and velocity difference amounting to 5 km s^{-1} across the Fabry-Perot field. Taking this into account, there appears to be a zero-point difference of 0.9 km s^{-1} between the two data sets. These differences may indicate a systematic problem with the Fabry-Perot calibration.

Calculation of the mean velocity differences for the full samples of the two comparisons gives dispersions about the means which are somewhat larger than expected if the adopted errors in each study are correct. Gebhardt et al. (1997) note that their measurement uncertainties are still not

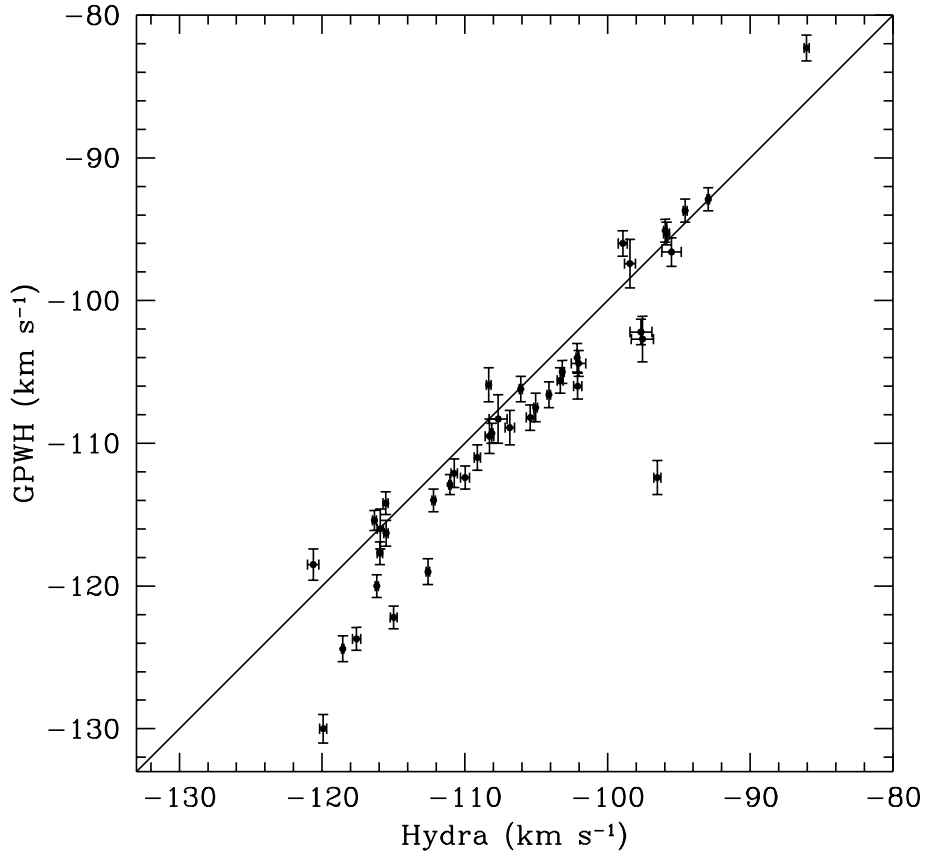


Fig. 4.— Comparison of our velocities with the Fabry Perot velocities of Gebhardt et al. (1994,1997).

fully understood, but the Peterson et al. uncertainties apparently are. Thus, in Figure 5 we show, against V magnitude, χ^2 for the two observations with respect to their mean for the comparison with Peterson et al. sample. There is a difference in behavior for stars on either side of $V = 13.3$. There appears to be extra variance for the stars brighter than $V = 13.3$. This is probably due to the velocity “jitter” seen for stars near the tip of the giant branch in many clusters (Gunn & Griffin 1979; Mayor et al. 1984; Lupton et al. 1987; Pryor et al. 1988). Peterson et al. (1989) attribute the excess variance in their repeat observations to an internal jitter of 0.88 km s^{-1} . The observations by Gebhardt et al. (1997) are generally not precise enough to see this effect. If we restrict our comparison to stars with $V > 13.3$ then the difference distribution is consistent with unit variance. This gives us confidence that our uncertainties have been calculated correctly. The question of the “jitter” will be addressed further in the next section.

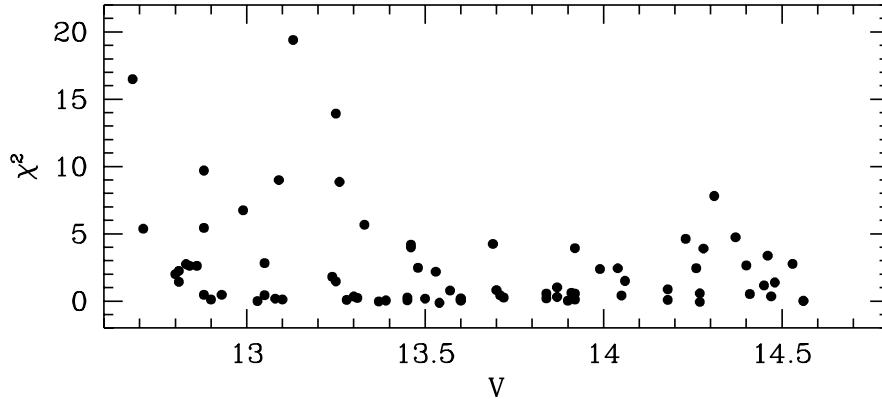


Fig. 5.— For the stars in common with Peterson et al. (1989) we show χ^2 vs. magnitude. Note the extra variance apparent for stars brighter than $V = 13.3$. This can be attributed to the jitter seen in the velocities of bright giants.

2.4. The Velocities

In total we have measured 1132 velocities for 591 stars in the field of M15. Figure 6 shows the measured velocities plotted against distance from the cluster center. This was taken to be $\alpha = 21^{\text{h}}29^{\text{m}}58^{\text{s}}.6$, $\delta = +12^{\circ}10'1''.0$ (J2000) (Guhathakurta et al. 1996). Generally, the cluster members stand out quite distinctly from the non-members based on the roughly 100 km s^{-1} velocity difference between the cluster and the foreground disk stars. We selected the cluster members by first excluding all stars with velocities greater than 40 km s^{-1} with respect to K1040. The spectra of all the rest of the stars were examined individually to estimate the equivalent widths of the Mg b lines. These lines are a sensitive luminosity indicator, but less so as a metallicity indicator (Geisler 1981), allowing us to distinguish between cluster giants and field dwarfs. All the stars with large equivalent widths were rejected as being field Population I dwarf stars. A few of the stars in the field region, those with the lowest velocities with respect to K1040, were also examined to check for high-velocity cluster members as have been seen in 47 Tuc (Meylan, Dubath, Mayor 1991). None was found. We also examined the spectra of 9 stars with velocities greater than 40 km s^{-1} with respect to K1040 that Cudworth (private communication) had assigned membership probabilities in excess of 50% based on their proper motions. All of these had high Mg b equivalent widths. There was also a population of a dozen stars with velocities significantly more negative than that of the cluster. Several of these had very weak spectra, which precluded estimates of the equivalent widths. Their velocities may be suspect. Most of the others had equivalent widths larger than the typical member, these are probable non-members. These have all been rejected from the cluster sample. These may be foreground halo dwarfs. There were also a few stars with velocities consistent with being cluster members, but spectra too poor to estimate the equivalent width. These have not been used in the subsequent analysis.

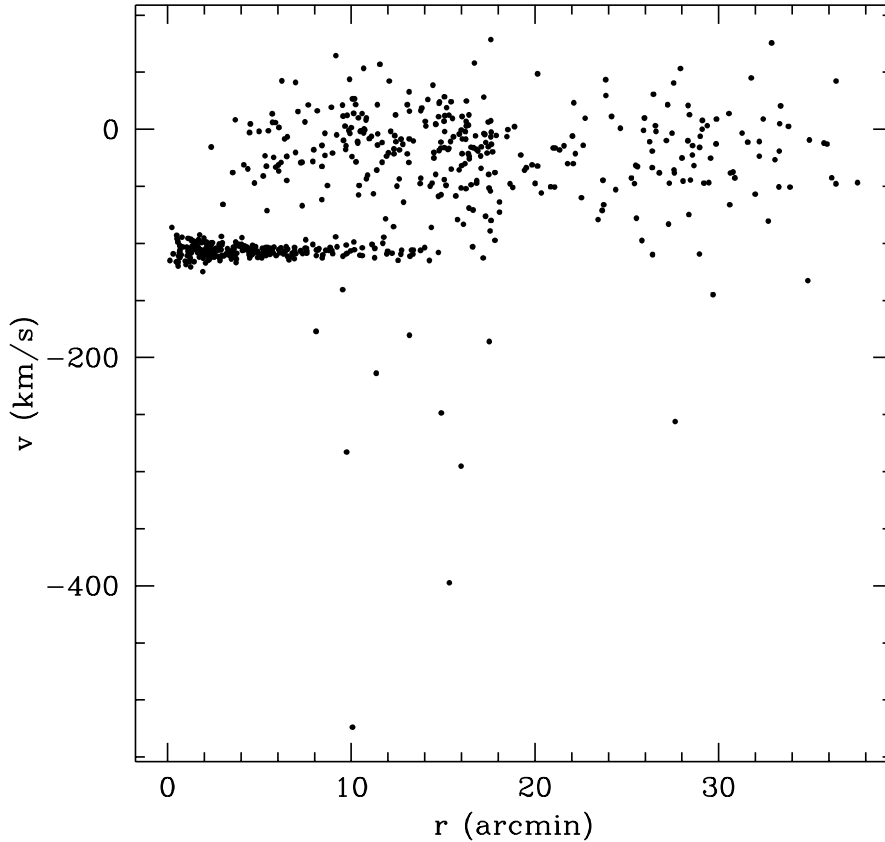


Fig. 6.— Velocities for all the stars observed in this study plotted against their radial positions. The cluster stands out as the clump with velocity near -107 km s^{-1} . The stars around zero velocity are disk stars, while the stars with very negative velocities probably belong to the halo.

In Table 2 we have listed the stars deemed to be members sorted by increasing right ascension. The first two columns are our coordinates for the stars with epoch 2000. The third column contains an identification to ease cross comparisons. For the stars from the Cudworth’s preliminary proper motion list, we have used his identifications from Küstner (1921), Aurière and Cordoni (1981), or from Sandage (1970). These can also be used for cross-identification with Peterson et al. (1989). For the rest of the stars we have used our own number from our master list of candidates. Further identification numbers for cross referencing with Gebhardt et al. (1997) are in the penultimate column. The fourth column is a V magnitude. The remaining columns are the number of observations for each star, the mean velocities, the uncertainties in the velocities (exclusive of the uncertainty in the velocity-zero point), and, for each star with more than one observation, the probability that the χ^2 of the differences of the observed velocities about their mean is consistent with no variability. The final column contains any notes. The velocities of the

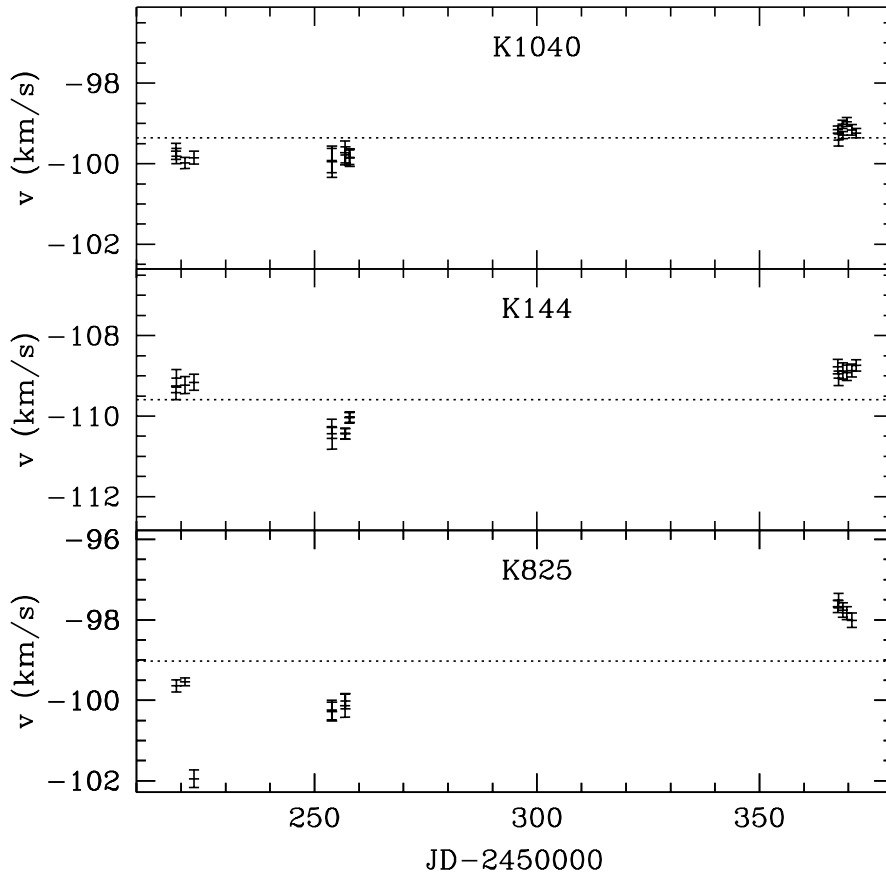


Fig. 7.— Velocity curves for the standard stars K1040 and K144 and for the suspected variable star K825. The errors shown do not include an allowance for jitter.

non-members are available from the authors.

We have compared our coordinates with the high precision astrometry of the inner $2'$ of M15 by Le Campion, Colin, & Geffert (1996). We find mean offsets (in the sense ours–Le Campion et al.) $\langle\Delta\alpha\rangle = -0.68'' \pm 0.23''$, $\langle\Delta\delta\rangle = +0.80'' \pm 0.22''$. Since their typical error is around $0.07''$, our relative astrometry is good to about $0.2''$. The mean offsets represent differences in the astrometric systems used in the studies. We use the *HST Guide Star Catalogue* as our reference, while Le Campion et al. use the FK5 system. The positions in the tables do not include the offset. The zero-point for our photometry has been determined by comparing stars in common between our list and Cudworth’s list, and shifting our magnitudes onto his system.

There are 17 stars in our member sample for which the probability of no velocity variability is less than 1%. Of these stars, 12 are in the upper one magnitude interval of the giant branch, here for $V < 13.6$, where it has long been suspected that the stars are subject to an intrinsic “jitter” in

their velocities of around 0.8 km s^{-1} (Gunn & Griffin 1979; Mayor et al. 1984; Lupton et al. 1987; Pryor et al. 1988). These include the two stars that we took as our velocity standards, K144 and K1040. Velocity curves for these two stars, plus K825, are shown in Fig. 7. Both show systematic variations between runs, but the velocities are consistent if a further 0.8 km s^{-1} is allowed for in the uncertainties. There are another 12 stars with 2 observations, 6 of these are at two epochs, which do not show any sign of this jitter. So it is unclear whether all bright giants suffer from this or what the time scale is of this variation. If we add 0.8 km s^{-1} in quadrature to the errors for all stars with $V < 13.6$, then 3 of these stars remain flagged as variables. These are marked by the note ‘b’ in Table 2. Those with now consistent velocities are marked ‘j’. The other five stars are fainter than this limit and have the note ‘v’. We provide the full set of velocities for the stars with ‘b’ and ‘v’ flags in Table 3. The star K673, which was claimed to be a binary by Gebhardt et al. (1994), only appears to be variable if the jitter is not included. The two observations in 1996 June and October differ by 0.8 km s^{-1} . Of the 8 stars we identify as velocity variables, 6 have only 2 observations, 4 of which are at two epochs. The star 5555 has a velocity difference of 16 km s^{-1} over a span of 3 days; star 6607 changes by 4.3 km s^{-1} over the same interval. The most extensive set of observations is for the star K825 which was noted to be variable in our 1996 May run. We present the velocity curve in Fig. 7. Most remarkable is a 2.4 km s^{-1} velocity change over the course of two days in our May observing run.

We will refer to the velocities without including the jitter factor as our ‘A’ sample. This consists of 213 non-variables and 17 variables. If we include the 0.8 km s^{-1} jitter factor in the velocity uncertainties of all the bright stars, then this ‘B’ sample consists of 222 non-variables and 8 variables. Only the non-variables in each sample will be used in estimating the mean, velocity dispersion profile, and rotation. In the analysis below we will use the A sample; the B sample gives very similar results.

Figure 8 shows our velocities plotted against radius. What is most striking is the apparent increase in the velocity dispersion beyond about $5'$. We will discuss this point in §4 using the methods described in the next section.

3. Bayesian Estimation

3.1. Introduction

We have a sample of velocities for members of the cluster, each with its own uncertainty. What we wish to measure are the mean velocity of the cluster and the velocity dispersion profile. The mean must be based on all of the velocities, but the velocity dispersion needs to be measured as a function of radius, in radial bins, for example. In addition, we often want to know if the observations indicate rotation and whether the rotation signal is significant. There are several approaches of increasing complexity which can be used to make these various measurements.

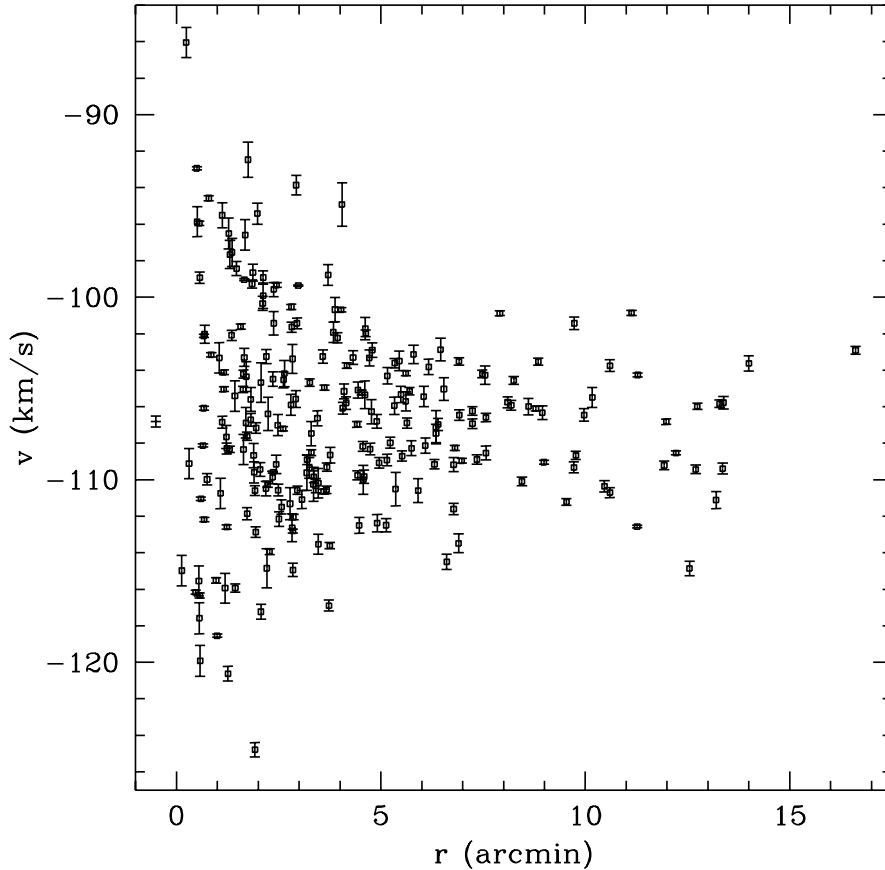


Fig. 8.— Velocities of the members of M15 plotted against radius. The velocity dispersion decreases as expected with radius until about $7'$. The velocity dispersion then appears to increase again. The point at negative radius indicates the inferred mean and its uncertainty. In this case the probability distribution is symmetric.

Peterson et al. (1989) used the simplest approach to calculating the mean and simply took an unweighted average of their 120 stellar velocities and derived the uncertainty from the scatter about the mean. This overstates the uncertainty since it will also include the unknown velocity dispersion of the cluster. They determined the velocity dispersion profile by dividing the sample into bins and taking the dispersion about the mean of the velocities in that bin as the local velocity dispersion. Again, the known and variable uncertainties in the velocities are ignored. Furthermore, the estimate of the cluster velocity based on the entire sample has also been ignored in determining the local velocity dispersion. The fractional error in the velocity dispersions was just taken as $1/\sqrt{2N}$ for a bin of N stars.

A more sophisticated approach is the maximum-likelihood method described by Pryor &

Meylan (1993). This assumes that the velocity for each star is drawn from a normal distribution with the standard deviation being the quadrature sum of the individual velocity uncertainty and the cluster velocity dispersion. Standard maximum-likelihood techniques result in equations for the mean and dispersion which can then be solved numerically. Pryor & Meylan also give equations for the variances of the derived quantities.

Another algorithm which has been used to measure the velocity dispersion profile utilizes the locally weighted scatter plot smoothing (LOWESS) algorithm (Cleveland & McGill 1984). First the cluster mean is estimated by some other method. Then the velocity variance at each data point is estimated in the following way, according to the application of this algorithm by Gebhardt et al. (1994). The squared deviations from the cluster mean are calculated. Then at each radius for which one wants to measure the dispersion: (1) A straight line is fit to these deviations as a function of radial position by weighted least-squares. The weights are the inverse squares of the differences of the stars in radial position, measured from the cluster center, with respect to the dispersion radius. (2) The square root of the fitted variance is taken as the velocity dispersion at that radius. The uncertainties in the velocity dispersions are calculated using a Monte Carlo method which assumes that the LOWESS dispersions are correct, but using the observed velocity uncertainties for individual stars. While this method does give a non-parametric estimate of the velocity dispersion profile, it suffers from calculating the mean and dispersions separately and from ignoring the measurement errors in calculating the velocity dispersion. Thus all velocities carry equal weight and the measurement of the velocity dispersion can be biased by single, highly-uncertain points with large deviations. To some extent this will be compensated for in estimating the uncertainty in the velocity dispersions, and more recent applications of the method have included the velocity uncertainty in the weighting (Gebhardt, private communication), but the robustness of this method has not been demonstrated.

Looking at the maximum-likelihood method from another perspective brings us to the Bayesian methods we employ here. The results are generally similar to those achieved with maximum likelihood, but there are several advantages. The Bayesian methods give probability distributions for the parameters, not just the most likely value and its variance. The Bayesian methods naturally incorporate any prior information on the values to be measured and also give the relative likelihood of various models. Thus, for example, we can decide whether a model including rotation is more or less likely than one without.

For discussions of the background of Bayesian analysis we refer the reader to Bretthorst (1988) and Press (1989). The classic source is Jeffreys (1961). Jaynes (1983) presents this material from a more modern perspective. Saha & Williams (1994) have used these methods in a somewhat different astronomical context.

In short, if we know the conditional probability of A given B , $P(A|B)$, then we can infer $P(B|A)$ using Bayes' theorem,

$$P(B|A) = \frac{P(A|B)P(B)}{P(A)}. \quad (2)$$

In eq. (2) $P(B)$ is referred to as the *prior probability* or the *prior*, it represents any information we have on the values of the parameters before we look at our data. $P(A|B)$ is the *likelihood*. $P(B|A)$ is the *posterior probability*; it is this we are seeking to measure. The final factor $P(A)$ is called the *global likelihood* and is a normalization factor.

A and B can represent data, models, model parameters and so on. In a Bayesian framework, the probabilities represent our state of knowledge. This is unlike the more familiar “frequentist” viewpoint which considers probabilities to just be the frequency with which something occurs. Here it is perfectly meaningful to discuss the probability of the parameters of a model having particular values. It is just as meaningful to compare the probability of two models. What is in question is not “How often will such a model occur?”, but “Given the previously known information and the data, what is the probability that this model is correct?” The prior represents our state of knowledge before making the observation. We may know nothing at all, in which case we would wish to choose as uninformative a prior as possible. Alternatively, we may have previous measurements which we are trying to refine. In this case, the proper prior is one which represents the previous measurements. We will see examples of both of these kinds of priors below. The appendices to Bretthorst (1988) contain some useful comments on the choice of priors.

If we have two different models, M_1 and M_2 , and we wish to choose between them, then the natural thing to look at is the posterior odds ratio

$$\frac{P(M_1|D)}{P(M_2|D)} = \frac{P(D|M_1)P(M_1)}{P(D|M_2)P(M_2)}, \quad (3)$$

where D is the data. If the number or nature of the parameters in the two models differ, it is important to keep all the normalization terms in the priors and likelihoods. If the odds ratio is greater than unity then model M_1 is favored, otherwise model M_2 is more likely. This will be used in discussing rotating and non-rotating models for the M15 data.

Since the notion of a posterior-odds ratio is unfamiliar, we feel that some further discussion is warranted to give a proper understanding of our results. Assume that $P_1(M_1|D)$ and $P_2(M_2|D)$ are the probability distributions for the values of two parameters, M_1 and M_2 given the data, and, further, assume that they are normal distributions with means μ_i and dispersions σ_i , where $i = 1, 2$. We can calculate the probabilities that $M_1 > M_2$ or that $M_1 < M_2$ and hence the odds of the two propositions. Define $k \equiv (\mu_1 - \mu_2)/\sqrt{\sigma_1^2 + \sigma_2^2}$. Then the odds of $M_1 > M_2$ over $M_1 < M_2$ are

$$\frac{1 + \operatorname{erf}\left(\frac{k}{\sqrt{2}}\right)}{1 - \operatorname{erf}\left(\frac{k}{\sqrt{2}}\right)}.$$

If $\mu_1 = \mu_2$, $k = 0$ and the odds are even; the two propositions are equally likely. For $k = 1$, a 1σ result, the odds are 5.3 to 1. That is, based on our prior knowledge and this data set, it is 5.3 times more likely that $M_1 > M_2$ than that $M_1 < M_2$. If μ_1 is 2σ larger than μ_2 the odds of $M_1 > M_2$ over $M_1 < M_2$ are 43 to 1. Similarly $k = 3$ gives odds of 740 to 1. If a horse in a horse race has odds of 5 to 1 against its winning, you wouldn’t be surprised if it won. Similarly, if the

posterior odds are 5 to 1 against M_2 being larger than M_1 you wouldn't be surprised if it really was larger. In general, we don't think of a 1σ result as being overly significant. If the odds were 740 to 1, we would be surprised if the horse won, or if, with additional data, M_2 proved to be larger than M_1 . But, we are similarly surprised if a 3σ result proves to be wrong. Nonetheless, it can be, and long-shots do sometimes win.

3.2. Velocity Models and Priors

Here we will look at several models for a globular cluster data sample, with different assumptions about the form of the velocity dispersion profile and about whether the cluster is rotating. The first pair of models assume a single mean velocity for the sample and then individual velocity dispersions for groups of stars binned by radius. The sizes of the bins are variable, we assume only that the velocity dispersion is the same for all stars in that radial bin. In effect we assume that the velocity dispersion can be approximated by a series of step functions. This is a general assumption of binning. First we will consider a model without rotation.

The data sample consists of N stellar velocities v_i each with uncertainty ϵ_i . The model parameters are the mean velocity \bar{v} and the set of velocity dispersions σ_r for the $r = 1, \dots, M$ radial bins. For a single observation we assume that the likelihood of observing v_i is given by

$$P(v_i|\bar{v}, \sigma_r, \epsilon_i) = \frac{1}{\sqrt{2\pi(\epsilon_i^2 + \sigma_r^2)}} \exp\left(-\frac{(v_i - \bar{v})^2}{2(\epsilon_i^2 + \sigma_r^2)}\right). \quad (4)$$

The likelihood of the whole data set D is

$$P(D|\bar{v}, \{\sigma_r\}, \{\epsilon_i\}) = \prod_i P(v_i|\bar{v}, \sigma_r, \epsilon_i). \quad (5)$$

Applying eq.(2) gives

$$P(\bar{v}, \{\sigma_r\} | D, \{\epsilon_i\}) \propto P(D|\bar{v}, \{\sigma_r\}, \{\epsilon_i\}) P(\bar{v}) \prod_r P(\sigma_r) \quad (6)$$

for the posterior probability. We have ignored the normalization factor $P(D)$ as we will only be concerned with the relative probabilities of various parameter combinations and, for different models of the same data, $P(D)$ is constant.

$P(\bar{v})$ and $P(\sigma_r)$ are the priors for the mean velocity and the velocity dispersion values. If we know nothing about the mean velocity then the appropriate prior to use is a uniform prior. In one sense this is a somewhat unusual probability distribution in that it is not normalizable. In practice this is not usually a problem. If we have a previous observation of the mean $\bar{v}_0 \pm \sigma_{\bar{v}_0}$, then we could use a normal distribution

$$P(\bar{v}) = \frac{1}{\sqrt{2\pi}\sigma_{\bar{v}_0}} \exp\left(-\frac{(\bar{v} - \bar{v}_0)^2}{2\sigma_{\bar{v}_0}^2}\right) \quad (7)$$

for the prior. The appropriate uninformative prior for a scale parameter such as the velocity dispersion σ_r is the Jeffreys (1961) prior σ_r^{-1} . (For a justification see Bretthorst 1988.)

An alternative model is one which allows for rotation in the data in addition to the mean and dispersion as in the previous model. One simple model is to assume a sinusoidal dependence of rotation velocity on azimuthal angle with a single position angle, ϕ_0 and amplitude A . We replace eq.(4) with

$$P(v_i, \phi_i | \bar{v}, \sigma_r, \phi_0, A, \epsilon_i) = \frac{1}{\sqrt{2\pi (\epsilon_i^2 + \sigma_r^2)}} \exp\left(-\frac{(v_i - [\bar{v} + A \sin(\phi_i - \phi_0)])^2}{2(\epsilon_i^2 + \sigma_r^2)}\right), \quad (8)$$

where ϕ_i is the position angle for observation i . The posterior probability is then

$$P(\bar{v}, \{\sigma_r\}, \phi_0, A | D, \{\epsilon_i\}) \propto P(D | \bar{v}, \{\sigma_r\}, \phi_0, A, \{\epsilon_i\}) P(\bar{v}) P(\phi_0) P(A) \prod_r P(\sigma_r). \quad (9)$$

The appropriate choice for the new priors is discussed in Bretthorst (1988). Based on his discussion we use

$$P(\phi_0) P(A) = \frac{1}{2\pi\delta^2} \exp\left(-\frac{A^2}{2\delta^2}\right). \quad (10)$$

The pseudo-dispersion δ is a *hyper-parameter*. This is a case where we can not use an improper, i.e. non-normalizable, prior as we want to compare the probabilities of the model with and without rotation. The other parameters with improper priors are common to both models, so their normalization divides out. The rotation parameters are only in one model and so their normalization must be taken into account for a proper comparison. We can see in the raw data (Figure 12) that any rotation for M15 must be small. This sets a limit on δ . The value we choose for δ expresses our estimate of the maximum amplitude of the rotation, the larger we choose δ to be, the larger the rotation signal must be to be considered significant with respect to the model without rotation.

As an alternative to a step-function for the velocity dispersion profile, we can consider a power-law form:

$$\sigma(r) = \sigma_0 r^\alpha. \quad (11)$$

This is still parametric, but does away with binning. The likelihood for a single observation is now

$$P(v_i | \bar{v}, \sigma_0, \alpha, \epsilon_i) = \frac{1}{\sqrt{2\pi (\epsilon_i^2 + \sigma_0^2 r^{2\alpha})}} \exp\left(-\frac{(v_i - \bar{v})^2}{2(\epsilon_i^2 + \sigma_0^2 r^{2\alpha})}\right), \quad (12)$$

and the posterior probability is

$$P(\bar{v}, \sigma_0, \alpha | D, \{\epsilon_i\}) \propto P(D | \bar{v}, \sigma_0, \alpha, \{\epsilon_i\}) P(\bar{v}) P(\sigma_0) P(\alpha). \quad (13)$$

The new priors are given by $P(\sigma_0) = \sigma_0^{-1}$, the Jeffrey's prior we saw above, and

$$P(\alpha) = \frac{1}{\sqrt{2\pi\gamma}} \exp\left(-\frac{(\alpha - \alpha_0)^2}{2\gamma^2}\right). \quad (14)$$

As in equation (10), α_0 and γ are hyper-parameters. Theory suggests $\alpha_0 = -0.5$, and we take $\gamma = 1$. The extension to the rotating case is straight forward.

3.3. Metropolis Algorithm

We calculate the posterior probability distributions using the Metropolis algorithm and follow the procedure in Saha & Williams (1994). The basic algorithm is as follows. We'll refer to a set of parameters as ϖ . (1) Start with some values of the parameters ϖ and calculate the posterior probability $P(\varpi|D)$. (2) Pick, at random from a uniform distribution, a possible change $\delta\varpi$ in the parameters and compute $P(\varpi + \delta\varpi|D)$. (3) If $P(\varpi + \delta\varpi|D) > P(\varpi|D)$ then replace ϖ by $\varpi + \delta\varpi$ for the next iteration. If not, replace ϖ by $\varpi + \delta\varpi$ with probability $P(\varpi + \delta\varpi|D)/P(\varpi|D)$. (4) Return to step (2) and iterate. The size of the trial changes must be large enough to ensure that the entire range of acceptable values of the parameters are covered, but be small enough that sufficient iterations accept change. Given enough iterations, the distribution of accepted values for the parameters converges to the posterior probability distribution.

In principle we should save each set of parameters to look at the full, multivariate distribution, but this would require too much memory and require too many iterations if the number of parameters is much larger than two. What we have done instead is to save the distribution of each parameter individually. This is equivalent to projecting the multivariate distribution along the axis of each parameter, that is, to calculating all the marginal probability distributions at the same time. Our estimator for each parameter is then the mode of the individual probability distribution. The posterior probability of the model is given by the overall probability using these estimators of the modes. With some multivariate probability distributions, it is possible for the peaks of the projected distributions to be significantly different from the global peak of the distribution. To help guard against this we also keep track during the iterations of the individual parameter sample giving the highest posterior probability. In general this set of parameters was close to, but not identical with the modes of the individual distributions; the posterior probabilities were similar. In practice, the distributions from our data sets are unimodal and strongly peaked, indicating that the modes of the projected distributions do represent fairly the peak of the multivariate distribution.

These projected posterior probability distributions for the various parameters were measured by counting the number of accepted parameter values on a grid. For a parameter x , $P_i\Delta x$ is the probability of x being between x_i and $x_i + \Delta x$, where the x_i are the grid points. We calculate the mode of $P(x|D)$ by finding the maximum value of P_i , at x_j say, and then using it and the two bracketing values to find the parabola $y(x)$ for which $\int_{x_i}^{x_i+\Delta x} y(x)dx = P_i\Delta x$ for each of $i = j - 1, j, j + 1$. The maximum of $y(x)$ is taken as the mode of the distribution. Using this interpolation form, the mode lies at

$$x = x_{j-1} + \frac{2P_{j-1} - 3P_j + P_{j+1}}{P_{j-1} - 2P_j + P_{j+1}}\Delta x \quad (15)$$

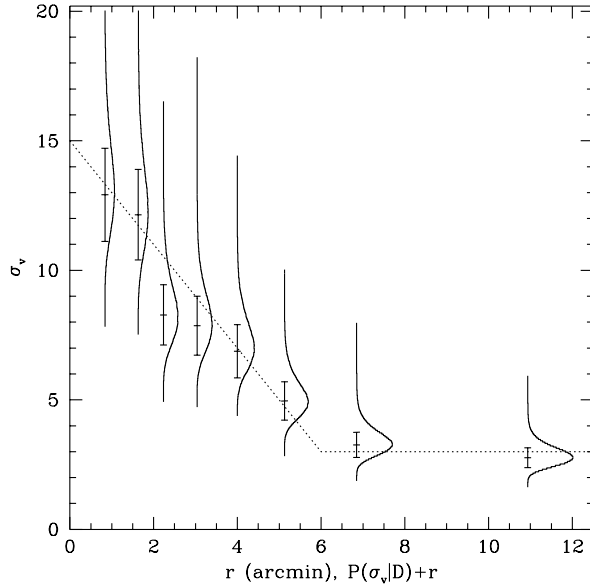


Fig. 9.— Velocity dispersion profile for the first example. The assumed velocity dispersion profile is shown as the dotted line. The histograms (turn the figure sideways) show the probability distributions for the velocity dispersion at that radius having the given value. The probability distributions are offset to have their zero levels at the mean radius of the star in the bin. This is the same position as the vertical line of the error bars for the accompanying points. The points represent the modes of the probability distribution and the error bars the symmetric region containing 68.5% of the probability. These can be thought of as 1σ error bars. Note that the probability distribution is really asymmetric; it is skewed to higher velocity dispersions. There is good agreement between the assumed profile and the estimated profile from the artificial data.

The number of iterations and the grid spacings for each parameter were chosen to ensure a smooth, well sampled distribution. Generally we used of order 10^6 samples to derive the posterior distributions.

3.4. Examples

We conclude this discussion with a couple of examples to demonstrate the method. For first example, we draw a sample of stars with the radii and errors of our ‘A’ sample. The velocities are drawn from a distribution with a mean velocity of -107 km s^{-1} and with a velocity dispersion profile that decreases linearly to $6'$, and then is constant beyond that, similar to the observed velocity dispersion profile. We then use the same parameters as in §4 to analyze this sample. The results are shown in Figure 9. The solid line is the assumed profile. The estimates of the velocity dispersions are displayed in two ways on this diagram: points with error bars and sideways

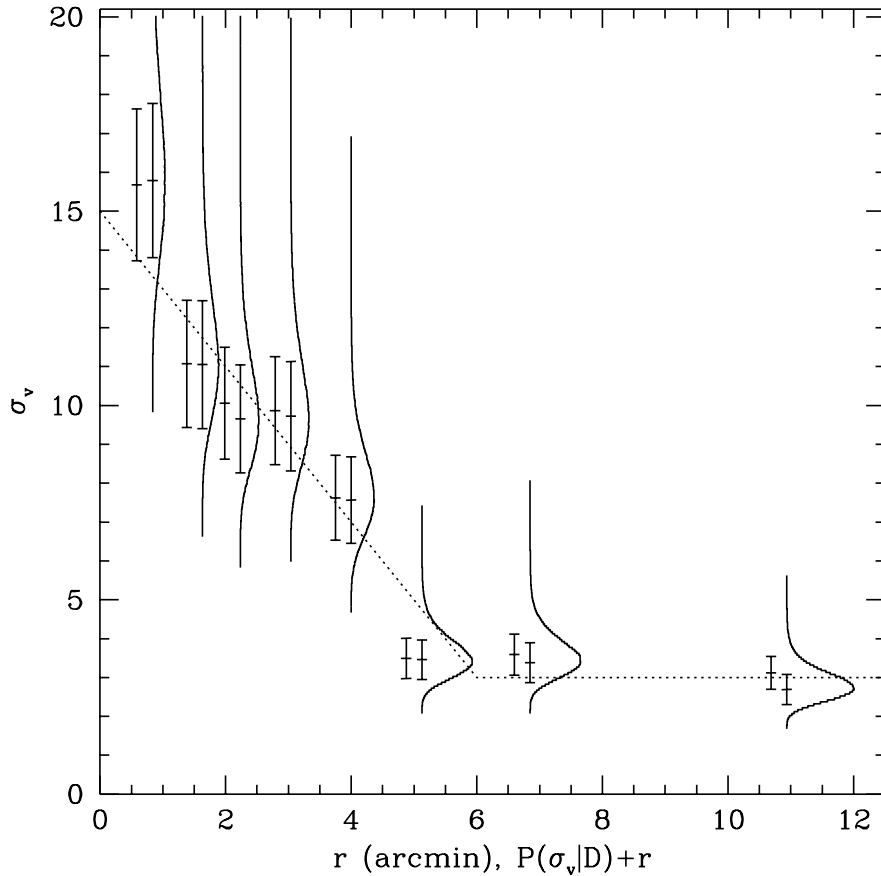


Fig. 10.— Velocity dispersion profile for the second example. The assumed velocity dispersion profile is shown as the dotted line. The curves and points are as described in Figure 9, except that we also show the mode and error bars for the solution without rotation. These are offset to the left.

histograms. The first displays the values in a traditional manner. The data points represent the mode of the distribution as discussed in §3.3. The error bars represent the symmetric region about the mode over which the integrated probability is 0.685. Thus, they are equivalent to 1σ errors. Note, however, that a symmetric probability integral is only one way of selecting the error region. Any contiguous region containing 68.5% of the probability would be equivalent. The agreement of the derived velocity dispersion profile with that assumed is quite satisfactory and the inferred mean velocity is $-107.0 \pm 0.3 \text{ km s}^{-1}$.

For our second example we draw the stars as before, but also assume the the entire cluster is rotating with amplitude 2 km s^{-1} and a position angle of 180° . We analyzed this result with both the rotating and non-rotating models. The rotation is estimated to have an amplitude of 1.7 ± 0.5

km s⁻¹ and position angle $176 \pm 19^\circ$. The mean is -106.7 ± 0.3 km s⁻¹. These all agree with the input model. The velocity dispersion profile is shown in Figure 10. There is general agreement between the estimates of the velocity dispersion and the assumed values. The model including rotation is a more likely fit to the data with odds of 10 to 1 in favor of rotation. This is only marginally significant, the data do not strongly support an interpretation of rotation. The sixth point may look to be too low, but full consideration of the statistics shows that this is not the case. The advantage of having the full probability distribution becomes apparent if we consider the odds ratio for this point to be greater or less than the assumed value at that radius. If we naively ignore the asymmetry and assume the probability distribution to have the mean and standard deviation shown, the difference is 2.5σ and the odds against the true value being higher than the assumed value are 173 to 1. If we use the measured probability distribution the odds are only 31 to 1, 5.5 times less unlikely, and equivalent to a 1.3σ difference for normally distributed errors.

4. Kinematics

4.1. Velocity dispersion profile

We now apply to our observations the methods discussed in the previous section. We begin by assuming that the cluster is not rotating. We divide the A sample into 7 bins of 26 stars each and an outermost bin of 31 stars, and run it through the Bayesian analyzer. The resulting mean velocity is -106.9 ± 0.3 km s⁻¹ assuming a uniform prior and -107.3 ± 0.2 km s⁻¹ if we use the Gebhardt et al. (1997) mean and uncertainty (-107.8 ± 0.3 km s⁻¹) as the prior. Our result in the latter case is just the average of the two measurements, exactly as we would have expected. The probability distribution of the mean velocity is well represented by a normal distribution with the quoted mean and dispersion.

Figure 11 shows the resulting velocity dispersion profile in the outer part of the cluster. If we use the B sample and just add the ‘jitter’ stars into the same radial bins, the results are much the same. The points and curves are as described for the examples in the previous section. The modes and the size of the symmetric error region are listed in Table 4. The radius given in the first column is just the mean radius of the stars in the bin. The histograms give the actual probability distributions for each velocity dispersion. These can be seen more clearly by turning the figure sideways. The zero level for the probability for each bin is the mean radius of the stars in the bin as represented by the vertical stroke of the error bars. It is clear that the probability distributions are skewed in all cases to higher velocity dispersions. It is more likely that the true dispersion is higher than the mode than less than it. This is easy to understand. It is always possible that the observed sample of stars lacks stars with large velocity differences from the mean, even if the underlying velocity distribution allows for such values. On the other hand, the stars with the largest velocity deviations in the sample put a much stronger lower limit on the velocity dispersion.

With the exclusion of the point at 4’, the velocity dispersion decreases with radius up to 5’.

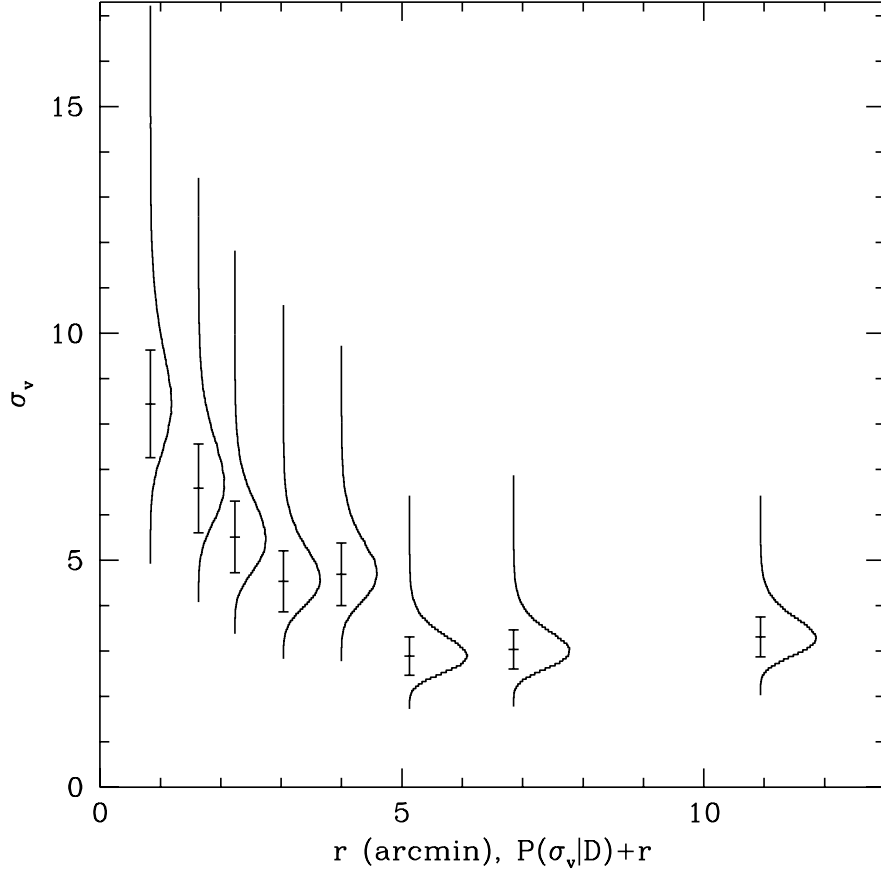


Fig. 11.— The inferred velocity dispersion profile assuming no rotation. The curves and points are as described in Figure 9.

Beyond this radius, the modes of the distributions increase again, confirming what is seen in the raw velocities. Since we have computed the probability distributions, it is straightforward to calculate the probability that one point is larger than another, or, alternatively, the odds. The probability that the last point is higher than the next-to-last is 67%, i.e. the odds are roughly 2 to 1 in favor of the last point being higher. For the last point and point at $5'$, the probability that the last is larger is 74% giving odds of 2.8 to 1. (For an explanation of these odds ratios, see the end of §3.1.) While intriguing, these results do not in themselves argue strongly for an increase in the velocity dispersion.

4.2. Rotation

It could be argued that the increase in the velocity dispersion is due to differences in the velocity tensor with radius. If the velocities are strongly tangentially anisotropic, the projected velocity dispersion would be higher than if the velocities are isotropically distributed. We discuss the case against tangential anisotropy in the next section, but since rotation has been claimed in the past for M15, here we look further at the special case of rotation. Gebhardt et al. (1997) find rotation with an amplitude of $2.1 \pm 0.4 \text{ km s}^{-1}$ and position angle $107 \pm 10^\circ$ for their overall sample.⁴ They also look at the variation with radius and find changes in both the amplitude and position angle.

Before continuing on to look for rotation in our sample, we need to address the question of “perspective rotation” arising from the proper motion of M15. This is discussed by Feast, Thackeray & Wesselink (1961) and more specifically with respect to ω Centauri by Merritt, Meylan & Mayor (1997). Simply put, the projection of the cluster’s space velocity along the lines of sight to various parts of the cluster results in an apparent rotation of the cluster, increasing with distance from the cluster center and varying inversely with the cluster distance. For ω Cen, which is at 5.2 kpc and has a total proper motion of $0.78 \text{ arcsec century}^{-1}$, the perspective rotation is about 1 km s^{-1} at $20'$. M15 is at 10.5 kpc; the value of its proper motion is disputed. Cudworth & Hanson (1993) measured an absolute proper motion of $\mu_\alpha \cos \delta = -0.03 \pm 0.10''/100a, \mu_\delta = -0.42 \pm 0.10''/100a$. Geffert et al. (1993) measured it to be $\mu_\alpha \cos \delta = -0.10 \pm 0.14''/100a, \mu_\delta = -1.02 \pm 0.14''/100a$. More recently Scholtz et al. (1996) derived a value of $\mu_\alpha \cos \delta = -0.01 \pm 0.04''/100a, \mu_\delta = +0.02 \pm 0.03''/100a$. None of these values agree, and the latest is effectively zero. Hence, we will ignore the effects of perspective rotation here.

If we use the rotating model for the velocities discussed in §3.2, assuming a single amplitude and position angle for the whole sample, then the mean velocity is the same. We have taken the hyper-parameter δ (see §3.2) to be 5 km s^{-1} . Rotation is detected. The amplitude is $1.5 \pm 0.4 \text{ km s}^{-1}$ and the axis of rotation is at $125 \pm 19^\circ$. The posterior odds ratio for a rotating model with respect to a non-rotation model is 15 to 1, indicating that the rotating model is more likely. This rotation is displayed in Fig. 12. The corresponding velocity dispersion profile, corrected for rotation, is shown in Fig. 13. For comparison, the modal values for the non-rotating analysis are shown as horizontal dashes offset to slightly smaller radii. Again, the modes and sizes of the symmetric error regions are given in Table 4. Rotation, if present, acts to increase the observed velocity dispersion if not accounted for. The large decrease in the velocity dispersion for the $4'$ point indicates that it is the stars at this radius that are most strongly affected by rotation. The dispersion at $7'$ also decreases somewhat for the rotating model. The probability that the last

⁴Gebhardt et al. define their position angle as the velocity maximum. We define ours as the rotation axis with the direction defined by right-handed rotation about it. We have subtracted the required 90° from their values to bring the definitions into agreement.

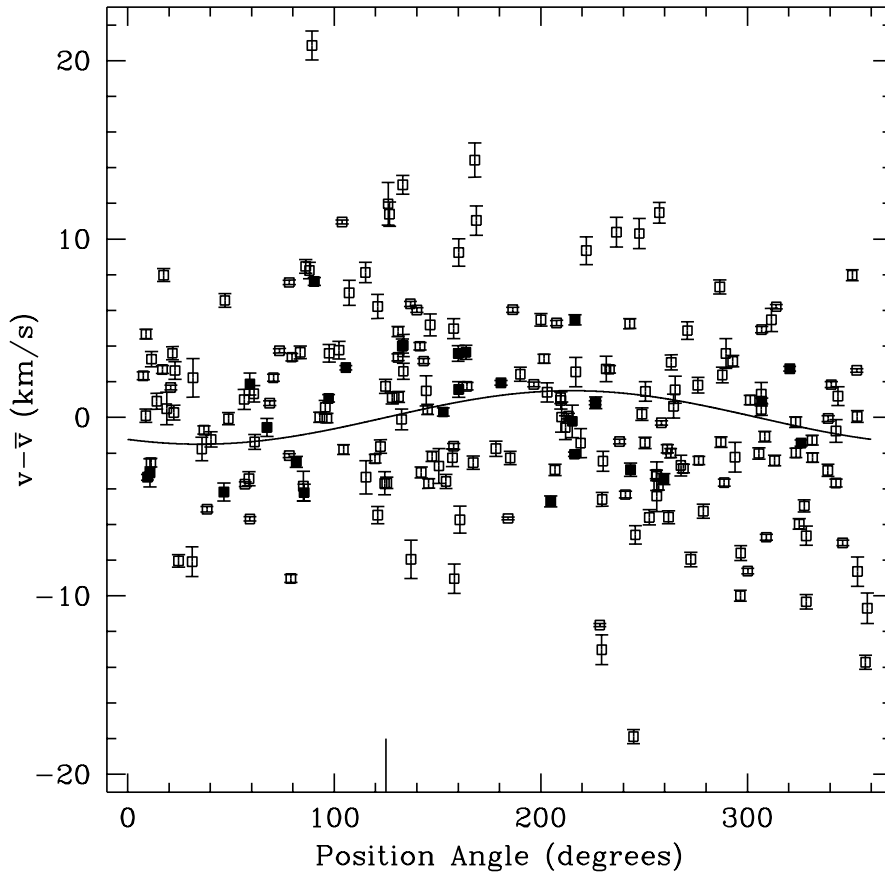


Fig. 12.— Observed velocities, less the cluster mean, as a function of position angle measured eastward from north. The inferred rotation is shown as the curve. The position angle of the rotation axis is indicated by the large tick mark. The stars in the 4' bin, which has the most significant rotation, are shown as filled symbols.

point is higher than the next-to-last is now 77%, i.e. the odds are roughly 3.3 to 1 in favor of the last point being higher, somewhat higher than for the case without rotation. For the last point and the point at 5', the probability that the last is larger is now only 65% giving odds of 1.8 to 1. The velocity dispersion now appears to reach its minimum closer to 7' rather than at 5' as in Fig. 11.

Since it has been claimed by Gebhardt et al. (1997) that the rotation properties change with radius, we have reanalyzed our sample by looking for rotation in each of our bins separately. We have kept the mean velocity fixed at -106.9 km s^{-1} . The results are shown in Table 5. Unlike Table 4, each bin is analyzed separately in this table. For each bin, as well as the overall sample analyzed in one bin (the line marked “All”), we give the dispersion without rotation and the

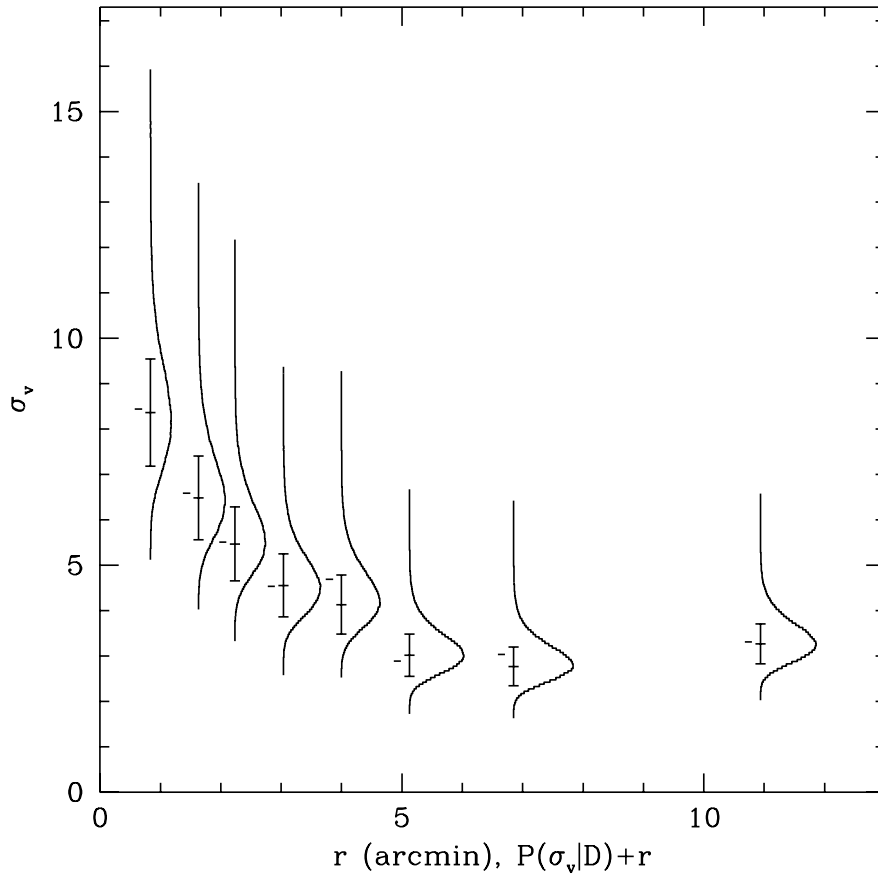


Fig. 13.— As Figure 10 for the velocity dispersion profile assuming there is rotation. The dispersion values from Figure 11 are shown a tick marks offset to the left of the new points. Note the decrease in the dispersion at 4'.

dispersion, rotation amplitude, and position angle assuming rotation. The final column gives the posterior odds ratio in the sense $P(\text{rotation}|D)/P(\text{no rotation}|D)$. Values larger than one indicate the model with rotation is more likely. For the bins where no rotation is detected, i.e. those with near zero amplitudes, the errors are the amplitude at which the integrated probability reaches 0.685, which corresponds to a 1σ upper limit. The only bin in which there is significant rotation detected is the one at 4' as we expected. The stars in this bin are highlighted in Figure 12. For a different binning, one with six bins alternating with 35 or 36 stars, no single bin shows significant rotation individually, yet the combined solution has posterior odds in favor of rotation of 33 to 1.

The proceeding results can be explained as a consequence of a subset of the observed velocities combining together to give the rotation signal. These stars are distributed across many of the bins and, depending on the binning, a given radial range may or may not show the rotation signal.

What the Bayesian posterior odds ratio gives is the strength with which one model is preferred over the other. In the last mentioned case, the rotating model with six bins is 33 times more likely to be a true description of the data than the non-rotating model with six bins. Similarly, for the original eight-bin model, the rotating model is about 15 times more likely than the non-rotating model. These are the same data; why the difference? This is a result of the interaction between the velocities of the stars in each bin and the dispersion and overall rotation in the model. Experiments with selections of radial sub-samples show that a group of 32 stars, including all of those in the 4' bin above, have a strong probability of rotation. In the six-bin model, these stars are divided into two bins and are combined with radially adjacent stars which do not support the rotation hypothesis as strongly. The individual bins do not show high probabilities of rotation, but the entire sample retains the signal. A recent Fokker-Planck study of rotating globular clusters shows that the rotation velocity should peak at an intermediate radius (Einsel & Spurzem 1997). Since the rotation amplitude is small, we would expect to detect it only where it is the strongest.

We conclude that our sample supports the view that rotation is present in M15. This rotation appears strongest near 4', but stars from the entire sample contribute to the signal. The sample is not large enough to look for radial changes in the rotation amplitude or position angle in a way independent of the binning. The ambiguities introduced by binning, characteristic of such a parametric approach, suggests that a non-parametric method would be a better way to resolve this question. In either case, more data are required.

Even if M15 does rotate, the amplitude is small and little rotation appears to occur outside 5', i.e. in the region where the velocity dispersion increases. Thus, rotation can not explain the increase in the velocity dispersion.

5. Discussion

Our observations of velocities in M15 indicate that the velocity dispersion reaches a minimum at a radius of around 7' and then appears to increase beyond this radius. Even if it does not increase, and the current data do not unequivocally require an increase, it is unlikely that the velocity dispersion continues to decrease at the rate expected for an isolated cluster. On theoretical grounds, we would expect the velocity dispersion to decrease with radius as a power-law for an isolated cluster, $\sigma(r) = \sigma_0 r^\alpha$, with a power-law index close to $\alpha = -0.5$.

To test this we have used the Bayesian algorithm to fit a model assuming a power-law relation for the velocity dispersion rather than the step function (i.e. a profile that is constant across each bin) used above. This model is also discussed in the Appendix. We have excluded the 31 stars in the final bin from the fit. For the model without rotation $\alpha = -0.46 \pm 0.08$ and for the model with rotation $\alpha = -0.48 \pm 0.08$. In both cases $\sigma_0 = 7.7$. For the 31 stars in the final bin, we calculated the posterior probabilities for the single-dispersion and power-law models, and hence the posterior odds ratio. Both without and with rotation, the dispersion calculated by the step-function model

is favored for the last bin. The odds against the power-law model are 165 to 1 without rotation and 320 to 1 with rotation.

This finding strongly suggest that there is an external energy source that heats the outer regions of the cluster and causes the observed deviation of the velocity dispersion profile from power-law behavior in the outermost part of the cluster. The most likely, and expected, energy source is tidal interaction with the galaxy. Whether the observed heating is due to the general galactic tide, or is due to shocks involving disk or bulge passages, is impossible to say given the current state of the observations and models.

But is an energy source necessary? While rotation has been ruled out, it could be argued that unorganized, *tangential* anisotropy could give the observed behavior of the velocity dispersion. This seems unlikely. Tonry (1983) has computed the velocity dispersion profile for spherical galaxies of varying anisotropy. Even for extreme tangential anisotropy, there is an increase in the velocity dispersion only inside of the effective radius of an $r^{1/4}$ law. Beyond this point, the velocity dispersion decreases, whatever the degree of anisotropy. Thus it is difficult to see how tangential anisotropy can increase the velocity dispersion in the outermost region of a globular cluster. Further, modeling of isolated globular clusters clearly demonstrates that the outer parts of such clusters would be strongly *radially* anisotropic (Larson 1970, Spitzer & Shull 1975, Cohn 1979). To convert this to tangential anisotropy would require external forces; those originating with the host galaxy. Thus, the explanation of tangential anisotropy, even if it could provide an increase in the velocity dispersion, and Tonry’s results suggest otherwise, still requires the influence of the galactic tidal field to change the orbits of the cluster stars. To convert radial orbits to circular orbits at the same apocenter requires energy input, i.e. tidal heating.

The increase in the velocity dispersion that we observe in the outer part of M15 is qualitatively very similar to that seen in the models of Allen & Richstone (1988). Their results suggest that the tidal radius should be identified as the location of the minimum velocity dispersion, at a radius of $7'$, which is very different from the $23'$ tidal radius measured by Grillmair et al. (1995). It is premature, however, to draw firm conclusions, since the theory of tidal heating and shocking has advanced since Allen & Richstone (1988). In particular, the recognition of the importance of the second order effects (Kundić & Ostriker 1995), and the new appreciation of the limitations of the assumption of adiabatic invariance (Weinberg 1994), require new models. Such modeling is well within current computational capabilities. What are required are models that can be compared with observations. If new models support the idea that the minimum in the velocity dispersion marks the edge of the region containing most of the bound stars, then our results are indeed in contradiction with the analysis of the surface density profile by Grillmair et al. (1996).

Besides new models, additional observations are also required in order to improve the statistical significance of our results and to clarify the role of rotation. We have observed virtually all the stars on the giant branch brighter than $V = 16.6$ outside the central region and inside $18'$. Below this magnitude, confusion with the galactic field becomes much stronger. Further out,

the fraction of members is similarly lower. While Hydra is an efficient instrument for observing large numbers of stars, better selection criteria, based for example on metallicity discriminating photometry using the Washington or DDO systems, are required. We have made such observations on the Washington system for the globular cluster M92, resulting in a striking increase in the fraction of stars in the sample selected for Hydra observation proving to be members. These observations will be presented in a future paper.

We thank K. Cudworth for the list of stars in his proper-motion program in advance of publication. We appreciate the support of grants from the Indiana University College of Arts and Sciences and Office of Research, and the University Graduate School.

REFERENCES

- Aguilar, L., Hut, P., & Ostriker, J.P. 1988, *ApJ*, 335, 720
- Allen, A.J. & Richstone, D.O. 1988, *ApJ*, 325, 583
- Aurière, M. & Cordoni, J.P. 1981, *A&AS*, 46, 347
- Bretthorst, G.L. 1988, *Bayesian Spectrum Analysis and Parameter Estimation* (Springer, New York)
- Capriotti, E.R. & Hawley, S.L. 1996, *ApJ*464, 765
- Cleveland, W. & McGill, R. 1984, *J. Am. Stat. Assoc.*, 79, 807
- Cohn, H. 1979, *ApJ*, 234, 1036
- Cudworth, K.M. & Hanson, R.B. 1993, *AJ*, 105, 168
- De Marchi, G. & Paresce, F. 1994, *ApJ*, 422, 597
- De Marchi, G. & Paresce, F. 1995, *A&A*, 304, 202
- Drukier, G. A. 1995, *ApJS*, 100, 347
- Drukier, G.A., Cohn, H.N., Lugger, P.M., & Yong, H. 1997, *ApJ*, submitted
- Dubath, P., Meylan, G. & Mayor, M. 1994, *ApJ*, 426, 192
- Dull, J.D, Cohn, H.N., Lugger, P.M., Murphy, B.W., Seitzer, P.O., Callanan, P.J., Rutten, R.G.M., & Charles, P.A. 1997, *ApJ*, 481, 267
- Einsel, C. & Spurzem, R. 1997, *MNRAS*, submitted, astro-ph/9704284
- Feast, M.W., Thackeray, A.D., & Wesselink, A.J. 1961, *MNRAS*, 122, 433
- Gebhardt, K., Pryor, C., Williams, T.B., & Hesser, J.E. 1994, *AJ*, 107, 2067 astro-ph/9402064
- Gebhardt, K., Pryor, C., Williams, T.B., Hesser, J.E., & Stetson, P.B. 1997, *AJ*, 113, 1026, astro-ph/9612116

- Geffert, M., Colin, J., Le Campion, J.-F., & Odenkirchen, M. 1993, *AJ*, 106, 168
- Geisler, D. 1981, *PASP*, 96, 723
- Gnedin, O.Y. & Ostriker, J.P. 1997, *ApJ*, 474, 223, astro-ph/9603042
- Grillmair, C.J., Freeman, K.C., Irwin, M., & Quinn, P.J. 1995, *AJ*, 109, 2553, astro-ph/9502039
- Grabhorn, R.P., Cohn, H.N., Lugger, P.M., & Murphy, B.W. 1992, *ApJ*, 392, 86
- Guhathakurta, P., Yanny, B., Schneider, D.B., & Bahcall, J. 1996, *AJ*, 111, 267, astro-ph/9512015
- Gunn, J.E. & Griffin, R.F. 1979, *AJ*, 84, 752
- Hut, P., McMillan, S., Goodman, J., Mateo, M., Phinney, E. S., Pryor, C., Richer, H.B., Verbunt, F. & Weinberg, M. 1992, *PASP*, 104, 981
- Jaynes, E.T. 1983, *Papers on Probability, Statistics, and Statistical Physics* (Reidel, Dordrecht)
- Jeffreys, H. 1961, *Theory of Probability* (Clarendon Press, Oxford)
- King, I.R. 1966 *AJ*, 71, 64
- King, I.R., Hedemann, E., Hodge, S.M., White, R.E. 1968 *AJ*, 73, 456
- Kundić, T. & Ostriker, J.P. 1995, *ApJ*, 438, 702
- Küstner, F. 1921, *Veröff. Sternw. Bonn.*, No. 15
- Le Campion, J.-F., Colin, J. & Geffert, M. 1996, *A&AS*, 119, 307
- Larson, R.B. 1970, *MNRAS*, 150, 93
- Lauer, T.R., et al. 1991, *ApJ*, 369, L45
- Lugger, P.M., Cohn, H.N., & Grindlay, J. 1995, *ApJ*, 439, 191
- Lupton, R., Gunn, J.E. & Griffin, R.F. 1987, *AJ*, 93, 1114
- Mayor, M., Benz, W., Imbert, M., Martin, N., Prevot, L., Anderson, J., Nordstrom, B., Ardeberg, A., Lindegren, H., & Maurice, E. 1984, *A&A*, 134, 118
- Meylan, G., Dubath, P., & Mayor, M. 1991, *ApJ*, 383, 587
- Merritt, D., Meylan, G., & Mayor, M. 1997, *AJ*, 114, 1074, astro-ph/9612184
- Oh, K.S. & Lin, D.N.C. 1992, *ApJ*, 365, 519
- Okazaki, T. & Tosa, M. 1995, *MNRAS*, 274, 480
- Peterson, R.C., Seitzer, P.O., & Cudworth, K.M. 1989, *ApJ*, 347, 251
- Press, S.J. 1989, *Bayesian Statistics: Principles, Models, and Applications* (Wiley, New York)
- Pryor, C., Latham, D., & Hazen, M. 1988, *AJ*, 96, 123
- Pryor, C. & Meylan, G. 1993, in *Structure and Dynamics of Globular Clusters*, S.G. Djorgovski & G. Meylan, eds. (Astronomical Society of the Pacific), p. 357
- Saha, P. & Williams, T.B. 1994, *AJ*, 107, 1295

- Sandage, A. 1970, ApJ, 162, 841
- Scholtz, R.-D., Odenkirchen, M., Hinte, S., Irwin, M.J., Borgen, F., & Ziener, R. 1996, MNRAS, 278, 251
- Sosin, C. & King, I.R. 1997, AJ, 113, 1328, astro-ph/9701030
- Spitzer, L. & Chevalier, R. 1973, ApJ, 183, 565
- Spitzer, L. & Shull, J.M. 1975, ApJ, 200, 339
- Tonry, J. & Davis, M. 1979, AJ, 84, 1511
- Weinberg, M. 1994, AJ, 108, 1398, astro-ph/9404015

TABLE 1. Observation Log

Setup Id	UT Date	Total Exp time (s)
central 1	1996 May 15	2400
central 2	1996 May 15	1800
K1	1996 May 17	4800
K2	1996 May 19	3000
A	1996 Jun 19	2100 ^c
B	1996 Jun 19	2100 ^c
C	1996 Jun 22	1800
D	1996 Jun 22	1800
E	1996 Jun 23	1800
F	1996 Jun 23	1800
H	1996 Oct 11	4500
N	1996 Oct 11	4800
I	1996 Oct 12	7200
O	1996 Oct 12	6000
P	1996 Oct 13	11500 ^c
Q	1996 Oct 14	4811 ^{c,d}
Q	1996 Oct 15	6000 ^d
R	1996 Oct 15	9300

^cObservations affected by clouds.

^dSpectra from both nights combined. Total exposure time 10811 s.

TABLE 2. Mean velocities of member stars

RA	(J2000)	DEC	Id	V	#	v	ϵ_v	$P(\chi^2)$	Other	Notes
21 29 5.12		+11 59 40.7	9494	14.90	3	-102.91	0.21	0.326		
21 29 8.40		+12 9 12.6	B5	13.57	3	-108.53	0.11	0.004		j
21 29 10.70		+12 16 37.7	9300	16.44	3	-105.78	0.35	0.249		
21 29 12.32		+12 10 50.6	B6	13.62	4	-112.56	0.07	0.034		
21 29 13.02		+12 11 15.7	C3	14.68	3	-100.86	0.14	0.058		
21 29 17.36		+12 16 37.2	C8	14.79	3	-106.82	0.15	0.272		
21 29 20.04		+12 14 0.6	8940	16.57	3	-105.49	0.54	0.153		
21 29 20.93		+12 13 22.0	8907	15.57	4	-101.43	0.35	0.995		
21 29 30.66		+12 10 38.0	8541	16.08	3	-109.17	0.38	0.697		
21 29 30.74		+12 6 33.3	K12	15.11	4	-106.59	0.23	0.811		
21 29 33.10		+12 12 51.6	K21	15.02	3	-111.60	0.31	0.887		
21 29 33.50		+12 4 56.0	K22	14.51	3	-100.88	0.13	0.649		
21 29 34.07		+11 59 39.4	8335	16.07	4	-109.21	0.24	0.124		
21 29 34.60		+12 3 20.0	K26	15.06	3	-103.53	0.19	0.701		
21 29 35.05		+12 6 4.3	K27	15.21	3	-106.45	0.29	0.032		
21 29 35.28		+12 14 8.9	K29	14.21	3	-108.96	0.13	0.740		
21 29 35.84		+12 8 28.1	K31	15.32	3	-105.15	0.21	0.250		
21 29 36.45		+12 3 55.4	K34	15.63	5	-105.75	0.30	0.497		
21 29 37.10		+12 13 41.3	8195	16.48	2	-107.12	0.92	0.753		
21 29 37.15		+12 8 9.8	8184	16.36	3	-105.33	0.44	0.753		
21 29 37.97		+12 11 58.9	K42	15.23	4	-103.61	0.26	0.100		
21 29 39.34		+12 12 39.4	8062	16.44	3	-105.95	0.48	0.111		
21 29 39.39		+12 18 21.6	8063	15.83	4	-111.22	0.18	0.244		
21 29 40.02		+12 16 0.7	K56	15.49	5	-104.20	0.21	0.902		
21 29 40.12		+12 5 19.6	8005	16.18	3	-102.87	0.62	0.530		
21 29 40.16		+12 8 24.0	8007	16.04	2	-103.32	0.44	0.722		
21 29 41.24		+12 7 20.1	K60	15.30	3	-109.08	0.29	0.525		
21 29 41.70		+12 3 37.8	K62	15.64	3	-108.53	0.38	0.683		
21 29 42.54		+12 7 28.0	7873	16.56	2	-101.71	0.61	0.411		
21 29 42.93		+12 9 54.2	K64	15.25	2	-108.65	0.43	0.253		
21 29 43.49		+12 10 4.1	K66	14.46	3	-104.96	0.14	0.781		
21 29 43.56		+12 15 48.0	K703	14.36	3	-108.25	0.14	0.619		
21 29 43.76		+12 6 16.2	7783	16.52	2	-104.31	0.45	0.622		
21 29 43.76		+12 8 34.0	K69	14.53	1	-101.92	0.56	...		
21 29 44.62		+12 7 31.4	K77	13.90	2	-103.74	0.15	0.335		
21 29 44.66		+12 5 8.4	7725	16.44	2	-110.59	0.65	0.338		
21 29 44.94		+12 6 31.0	K81	15.71	4	-102.90	0.40	0.833		
21 29 45.78		+12 8 46.2	K87	13.87	3	-108.52	0.16	0.290		
21 29 46.03		+12 11 32.2	K89	14.56	1	-109.84	0.32	...		
21 29 46.67		+12 3 21.4	K92	15.28	4	-106.23	0.23	0.008		v
21 29 46.74		+12 16 18.4	7586	16.56	3	-113.48	0.51	0.666		
21 29 46.84		+12 11 45.7	K97	15.17	1	-107.47	0.67	...		
21 29 46.86		+12 12 58.3	7573	16.11	4	-106.08	0.33	0.142		
21 29 46.91		+12 8 27.3	K95	14.87	1	-109.62	0.97	...		
21 29 47.35		+12 9 5.3	K105	15.37	1	-112.63	0.76	...		
21 29 47.82		+12 6 44.8	7490	15.90	2	-105.80	0.34	0.588		
21 29 47.83		+12 8 46.1	K114	13.92	2	-112.81	0.11	0.000		v
21 29 47.91		+12 5 48.9	7483	16.37	2	-112.38	0.48	0.087		
21 29 48.50		+12 20 20.5	7463	16.18	3	-110.71	0.27	0.659		
21 29 48.53		+12 6 44.6	7440	16.50	1	-94.92	1.19	...		
21 29 48.59		+12 11 46.4	K129	14.31	2	-101.43	0.29	0.818		
21 29 48.69		+12 6 39.1	7427	15.97	2	-105.16	0.40	0.152		
21 29 48.81		+12 10 25.9	K133	15.17	3	-104.48	0.39	0.072		
21 29 49.09		+12 9 4.4	K136	14.85	1	-109.16	0.50	...		
21 29 49.67		+12 9 24.1	K141	14.98	2	-103.25	0.39	0.802		
21 29 49.75		+12 11 6.6	K144	13.09	16	-109.59	0.04	0.000		j
21 29 49.76		+12 12 30.6	K145	15.39	1	-109.35	0.56	...		
21 29 49.89		+12 18 12.9	K153	15.53	4	-110.09	0.24	0.443		
21 29 49.91		+12 8 5.9	K146	13.60	2	-100.53	0.14	0.493		
21 29 49.91		+12 14 7.6	K150	15.53	2	-109.83	0.37	0.771		

TABLE 2. (continued)

RA (J2000)	DEC	Id	V	#	v	ϵ_v	$P(\chi^2)$	Other	Notes
21 29 50.07	+12 15 43.1	7328	16.57	2	-105.44	0.55	0.303		
21 29 50.10	+12 7 52.9	K151	15.08	1	-93.86	0.53	...		
21 29 50.12	+12 9 34.0	K154	14.92	1	-109.44	0.37	...		
21 29 50.14	+12 6 41.4	K152	15.26	1	-100.68	0.67	...		
21 29 50.24	+12 9 3.6	K158	14.28	1	-110.49	0.40	...		
21 29 50.48	+12 20 18.9	C18	14.91	2	-110.36	0.31	0.755		
21 29 51.30	+12 9 39.2	K181	15.10	1	-92.47	0.96	...		
21 29 51.39	+11 56 50.7	7186	15.81	4	-105.83	0.21	0.796		
21 29 51.43	+12 8 11.2	K185	14.56	1	-107.01	0.58	...		
21 29 51.51	+12 11 58.4	7204	15.61	2	-111.49	0.39	0.690		
21 29 51.61	+12 12 5.0	K197	15.23	1	-104.18	0.72	...		
21 29 51.67	+12 8 30.8	7179	14.74	1	-114.85	1.07	...		
21 29 51.81	+12 14 28.9	7174	15.74	2	-108.32	0.32	0.529		
21 29 51.82	+12 8 56.1	K205	14.93	2	-110.60	0.27	0.489		
21 29 51.86	+12 6 39.5	K202	15.20	1	-98.78	0.57	...		
21 29 52.27	+12 19 40.4	C20	15.51	5	-108.66	0.23	0.361		
21 29 52.28	+12 10 52.1	K224	13.39	1	-106.88	0.84	...		
21 29 52.41	+12 6 59.2	7108	15.55	1	-110.25	0.93	...		
21 29 52.41	+12 7 59.3	K228	15.03	3	-110.57	0.32	0.193		
21 29 52.61	+12 10 44.6	K238	13.24	2	-101.61	0.15	0.129		
21 29 52.64	+12 4 40.6	7081	15.60	3	-108.70	0.28	0.024		
21 29 52.72	+12 11 2.4	K240	12.93	1	-104.35	0.82	...		
21 29 52.81	+12 14 16.7	7084	16.54	3	-112.50	0.43	0.224		
21 29 53.08	+12 12 31.8	K255	13.87	1	-101.64	0.28	...		
21 29 53.11	+12 11 3.2	K254	13.28	1	-108.34	0.82	...		
21 29 53.27	+12 4 21.2	7036	16.34	3	-103.13	0.50	0.398		
21 29 53.27	+12 9 34.7	K260	13.99	1	-97.66	0.77	...	Geb 1463	
21 29 53.54	+12 9 11.3	K272	13.48	1	-105.41	0.84	...	Geb 1526	
21 29 53.76	+12 10 21.0	K288	13.71	2	-105.04	0.13	0.043	Geb 1369	
21 29 53.80	+12 9 34.5	K290	13.37	1	-115.94	0.82	...	Geb 1397	
21 29 54.16	+12 10 55.6	K309	14.95	1	-97.55	0.78	...	Geb 1490	
21 29 54.67	+12 1 6.7	6921	16.42	3	-106.33	0.38	0.614		
21 29 54.69	+12 8 59.9	K328	13.70	1	-102.09	0.28	...	Geb 1484	
21 29 54.90	+12 13 23.2	K341	12.86	1	-110.19	0.81	...		
21 29 54.96	+12 11 45.4	6914	14.29	2	-124.79	0.39	0.162		
21 29 55.01	+12 2 49.2	K337	14.86	3	-106.93	0.26	0.069		
21 29 55.25	+12 16 8.6	6894	16.41	2	-103.81	0.42	0.042		
21 29 55.32	+12 15 5.9	6883	15.67	3	-112.49	0.36	0.048		
21 29 55.43	+12 11 4.9	K373	12.88	1	-96.51	0.84	...	Geb 1443	
21 29 55.56	+12 9 7.4	K383	13.82	1	-95.51	0.68	...	Geb 1347	
21 29 55.57	+12 12 42.9	K387	13.53	1	-111.31	0.87	...		
21 29 55.59	+12 10 46.2	K386	12.80	2	-118.54	0.08	0.063	Geb 1266	
21 29 55.61	+12 11 43.1	6852	15.62	2	-106.72	0.35	0.479		
21 29 55.69	+12 11 34.5	K393	13.31	1	-96.59	0.84	...		
21 29 55.72	+12 7 59.7	6838	15.66	1	-99.92	0.70	...		
21 29 55.87	+12 9 33.2	K406	13.81	1	-109.98	0.31	...	Geb 1048	
21 29 56.14	+12 10 18.4	K421	12.71	2	-111.04	0.09	0.000	Geb 847	j
21 29 56.15	+12 12 34.5	K431	13.08	2	-107.20	0.12	0.016		
21 29 56.26	+12 9 55.0	K435	13.50	1	-95.86	0.82	...	AC 529	
21 29 56.35	+12 14 45.9	6791	16.35	2	-106.27	0.67	0.611		
21 29 56.41	+12 10 30.0	K447	13.25	2	-106.08	0.11	0.882	Geb 945	
21 29 56.53	+12 11 56.8	K460	15.18	1	-95.42	0.58	...		
21 29 56.63	+12 9 47.0	K462	12.90	2	-116.16	0.11	0.000	AC 13	j
21 29 56.67	+12 14 36.3	6763	16.18	3	-105.35	0.76	0.095		
21 29 56.69	+12 13 11.3	K476	14.67	2	-108.90	0.26	0.026		
21 29 56.76	+12 10 27.5	K479	12.68	1	-119.92	0.84	...	Geb 824	
21 29 56.99	+12 9 38.2	K490	12.84	2	-92.94	0.08	0.000	AC 463	j
21 29 57.02	+12 8 53.7	K488	13.46	2	-104.11	0.12	0.775	Geb 1376	
21 29 57.11	+12 4 22.8	K486	15.49	3	-106.89	0.28	0.931		
21 29 57.36	+12 10 38.5	K511	13.10	2	-102.12	0.09	0.000	AC 808	j

TABLE 2. (continued)

RA	(J2000)	DEC	Id	V	#	v	ϵ_v	$P(\chi^2)$	Other	Notes
21 29 57.40	+12 8 22.1	K506	14.77	1	-103.30	0.49	...			
21 29 57.76	+12 9 28.6	K531	13.05	2	-95.95	0.11	0.011	Geb 792		
21 29 57.98	+12 14 26.9	K553	14.96	3	-109.76	0.24	0.584			
21 29 58.00	+12 11 54.9	K550	15.12	1	-109.59	0.58	...			
21 29 58.25	+12 8 10.1	K560	14.27	2	-99.28	0.22	0.749			
21 29 58.27	+12 4 33.7	6607	16.41	2	-103.49	0.54	0.000			v
21 29 58.29	+12 9 13.4	K567	13.25	2	-94.57	0.14	0.000	Geb 1087		j
21 29 58.31	+12 9 46.6	K570	13.05	1	-86.05	0.82	...	AC 411		
21 29 58.35	+12 10 42.2	K578	13.72	1	-102.03	0.50	...	Geb 968		
21 29 58.53	+12 9 22.0	K583	12.83	2	-108.12	0.09	0.000	Geb 924		b
21 29 58.56	+12 8 8.6	K582	14.48	1	-98.66	0.46	...			
21 29 58.68	+12 8 56.7	K589	13.45	1	-110.75	0.83	...	Geb 1315		
21 29 58.70	+12 8 32.9	K592	14.05	1	-98.43	0.38	...	Geb 1539		
21 29 58.77	+12 9 56.8	AC 111	13.33	1	-114.98	0.84	...			
21 29 58.81	+12 10 17.9	AC 761	13.45	1	-109.12	0.83	...			
21 29 59.28	+12 9 12.3	K634	12.81	2	-103.16	0.12	0.334	Geb 1141		
21 29 59.42	+12 8 36.1	K647	13.60	1	-115.93	0.22	...	Geb 1529		
21 29 59.75	+12 11 0.5	K670	13.13	1	-103.32	0.83	...	Geb 1295		
21 29 59.78	+12 11 11.4	K672	13.84	1	-108.28	0.30	...	Geb 1420		
21 29 59.80	+12 9 26.4	K673	13.17	2	-112.18	0.11	0.006	Geb 972		j
21 29 59.85	+12 12 29.6	K682	15.32	2	-112.15	0.40	0.944			
21 29 59.95	+12 6 27.3	K677	15.09	2	-103.25	0.36	1.000			
21 30 0.00	+12 13 40.4	K691	14.65	3	-109.31	0.23	0.453			
21 30 0.24	+12 9 41.6	K706	13.03	2	-116.33	0.14	0.000	Geb 809		b
21 30 0.24	+12 14 25.7	K714	15.23	3	-105.09	0.44	0.583			
21 30 0.30	+12 10 51.4	K702	12.99	2	-115.51	0.15	0.065	Geb 1241		
21 30 0.34	+12 7 37.1	K709	13.69	2	-99.33	0.13	0.493			
21 30 0.54	+12 10 4.8	K733	13.30	1	-115.54	0.82	...	AC 11		
21 30 0.58	+12 10 2.1	K734	13.26	1	-117.59	0.85	...	AC 650		
21 30 0.59	+12 10 6.4	K735	13.73	1	-98.93	0.31	...	AC 651		
21 30 0.63	+12 22 33.2	6442	16.49	3	-114.86	0.40	0.094			
21 30 0.87	+12 8 57.8	K757	12.88	2	-112.59	0.12	0.110	Geb 1423		
21 30 1.08	+12 7 15.8	K769	15.59	2	-103.38	0.80	0.003			v
21 30 1.11	+12 12 18.0	K776	15.46	2	-99.58	0.39	0.693			
21 30 1.60	+12 12 30.8	K800	14.71	1	-104.52	0.44	...			
21 30 2.22	+12 11 22.4	K825	12.81	12	-99.03	0.05	0.000			b
21 30 2.60	+11 56 51.3	6246	16.49	3	-111.11	0.47	0.801			
21 30 2.70	+12 10 44.5	K853	12.88	2	-108.33	0.17	0.860	Geb 1454		
21 30 2.73	+12 6 56.6	K846	14.06	1	-104.68	0.20	...			
21 30 2.75	+12 11 28.5	6256	15.55	1	-105.60	0.66	...			
21 30 2.86	+12 10 8.9	K863	13.92	1	-106.85	0.33	...	Geb 1340		
21 30 3.06	+12 10 22.4	K866	14.70	1	-107.66	0.63	...	Geb 1415		
21 30 3.14	+12 13 29.5	K875	14.18	2	-110.55	0.20	0.964			
21 30 3.45	+12 10 4.7	K884	14.17	1	-120.62	0.40	...	Geb 1439		
21 30 3.47	+12 3 13.1	K879	14.20	3	-103.52	0.21	0.203			
21 30 3.97	+12 8 58.5	K902	14.89	2	-107.61	0.23	0.127			
21 30 4.07	+12 7 27.7	K906	15.19	1	-105.57	0.46	...			
21 30 4.18	+12 8 28.3	K912	14.45	1	-100.34	0.38	...			
21 30 4.28	+12 10 56.8	K919	13.60	1	-111.86	0.34	...			
21 30 4.58	+12 8 54.4	K925	14.55	1	-108.67	0.66	...			
21 30 4.59	+12 10 33.4	K928	13.92	1	-105.06	0.17	...			
21 30 4.62	+12 7 41.2	K926	15.25	2	-105.89	0.57	0.110			
21 30 4.71	+12 9 32.4	6080	13.90	1	-104.21	0.22	...			
21 30 4.71	+12 11 10.9	K932	14.09	1	-107.16	0.29	...			
21 30 4.77	+12 11 47.6	K934	14.47	1	-101.43	0.65	...			
21 30 4.81	+12 11 7.6	K936	14.23	1	-112.87	0.29	...			
21 30 5.15	+12 13 21.0	K947	14.37	1	-116.89	0.30	...			
21 30 5.50	+12 8 56.0	K954	14.40	1	-104.68	1.08	...			
21 30 5.51	+12 11 5.8	K956	14.54	1	-117.23	0.40	...			
21 30 5.54	+12 7 6.0	K953	15.40	2	-110.33	0.39	0.207			

TABLE 2. (continued)

RA	(J2000)	DEC	Id	V	#	v	ϵ_v	$P(\chi^2)$	Other	Notes
21 30	5.82	+12 1 13.1	K957	13.87	4	-109.04	0.10	0.535		
21 30	6.23	+11 56 47.8	5934	15.71	4	-109.39	0.30	0.877		
21 30	6.33	+12 7 0.0	K969	13.54	2	-110.64	0.13	0.402		
21 30	6.57	+12 9 22.9	K973	15.42	1	-98.92	0.36	...		
21 30	6.93	+12 7 47.3	K979	14.26	2	-111.08	0.50	0.752		
21 30	6.95	+12 9 17.2	K981	15.25	1	-106.40	0.91	...		
21 30	7.26	+12 10 51.5	K989	15.15	2	-109.87	0.34	0.417		
21 30	7.31	+12 9 38.5	K990	13.84	2	-110.25	0.16	0.867		
21 30	7.36	+12 10 33.7	K993	14.04	3	-113.93	0.16	0.339		
21 30	7.46	+12 8 14.3	K994	13.91	3	-112.04	0.15	0.539		
21 30	7.99	+12 12 55.1	K1006	14.27	2	-113.61	0.17	0.332		
21 30	8.23	+12 4 8.9	5778	16.41	3	-107.46	0.50	0.718		
21 30	8.91	+12 8 49.9	K1014	14.78	1	-114.94	0.36	...		
21 30	9.52	+12 4 57.9	5668	16.31	4	-108.27	0.41	0.193		
21 30	9.68	+12 13 43.2	K1029	13.57	2	-101.97	0.18	0.542		
21 30	9.76	+12 12 55.1	K1030	14.23	3	-100.69	0.12	0.115		
21 30	9.86	+12 10 53.2	K1033	14.41	2	-110.57	0.22	0.213		
21 30	10.40	+12 11 49.6	5612	15.12	2	-113.53	0.54	0.391		
21 30	10.47	+12 10 7.0	K1040	13.46	17	-99.36	0.03	0.000		j
21 30	10.48	+12 15 54.8	5613	16.26	3	-114.50	0.42	0.306		
21 30	10.55	+12 14 12.1	K1042	15.44	4	-108.92	0.32	0.932		
21 30	11.20	+12 14 20.8	5555	15.84	2	-110.51	0.92	0.000		v
21 30	11.27	+12 1 49.3	K1049	14.65	4	-106.10	0.13	0.560		
21 30	11.35	+12 8 42.1	K1054	14.24	1	-106.63	0.41	...		
21 30	11.60	+12 14 6.5	5523	15.64	3	-107.97	0.30	0.484		
21 30	12.00	+12 4 23.7	5479	16.08	3	-105.03	0.62	0.773		
21 30	14.23	+12 9 24.4	K1069	14.61	2	-102.23	0.28	0.254		
21 30	14.68	+12 12 11.8	K1071	15.59	3	-108.17	0.27	0.272		
21 30	14.71	+12 8 25.0	K1070	15.36	3	-103.30	0.37	0.171		
21 30	15.19	+12 19 46.9	5304	15.64	3	-103.75	0.32	0.705		
21 30	15.20	+12 11 35.4	K1074	15.26	5	-106.96	0.16	0.063		
21 30	15.54	+12 5 12.0	K1076	15.48	4	-106.97	0.34	0.715		
21 30	15.62	+12 8 23.8	K1079	14.18	3	-105.22	0.13	0.562		
21 30	15.75	+12 17 0.4	K1083	15.45	3	-105.92	0.26	0.046		
21 30	16.04	+12 13 35.0	K1084	14.51	3	-104.17	0.14	0.725		
21 30	16.65	+12 9 9.8	5205	16.48	2	-110.00	0.79	0.879		
21 30	17.30	+12 6 4.9	5168	16.20	3	-108.13	0.42	0.450		
21 30	18.11	+12 9 15.9	5138	15.62	4	-106.80	0.38	0.581		
21 30	20.34	+12 11 34.3	5044	16.53	2	-105.71	0.53	0.670		
21 30	21.00	+12 13 1.5	K1097	15.50	3	-109.15	0.26	0.654		
21 30	22.49	+12 14 23.2	K1104	15.56	5	-108.89	0.26	0.625		
21 30	22.68	+12 18 0.4	K1106	14.70	2	-106.45	0.34	0.944		
21 30	25.55	+12 17 6.0	4796	15.84	3	-109.32	0.30	0.458		
21 30	26.77	+12 7 4.8	4724	16.22	3	-104.27	0.50	0.676		
21 30	29.64	+12 20 11.8	B18	13.96	3	-105.98	0.17	0.878		
21 30	31.75	+12 8 55.7	K1136	14.85	3	-104.56	0.22	0.917		
21 30	32.48	+12 7 54.8	4483	15.97	4	-105.99	0.45	0.233		
21 30	44.10	+12 11 23.5	B30	13.75	4	-104.26	0.10	0.096		
21 30	49.26	+12 7 32.1	C35	15.11	5	-109.43	0.24	0.609		
21 30	54.39	+12 7 11.5	3599	16.49	4	-103.63	0.42	0.620		

Notes to Table 2.

b: Star remains variable if jitter of 0.8 km s^{-1} is included. j: Star is not variable if jitter of 0.8 km s^{-1} is included. v: Variable star fainter than jitter limit.

TABLE 3. Repeat observations of possible variables

JD	v	ϵ_v	JD	v	ϵ_v
K92			K825		
2450218.892	-105.87	0.43	2450218.962	-99.64	0.15
2450220.927	-109.69	1.07	2450220.927	-99.54	0.10
2450222.931	-105.77	0.57	2450222.931	-101.95	0.22
2450371.704	-106.26	0.32	2450253.857	-100.24	0.24
K114			2450253.924	-100.28	0.23
2450218.962	-113.65	0.25	2450256.877	-100.13	0.29
2450371.704	-112.62	0.12	2450256.935	-100.02	0.19
6607			2450367.633	-97.67	0.15
2450368.778	-95.41	1.02	2450367.782	-97.52	0.18
2450371.704	-104.70	0.64	2450368.778	-97.76	0.18
K583			2450369.603	-97.83	0.16
2450253.857	-111.97	0.30	2450370.753	-98.01	0.18
2450371.704	-107.77	0.09	5555		
K706			2450368.778	-98.71	1.78
2450256.877	-118.13	0.22	2450371.704	-114.86	1.08
2450368.778	-115.12	0.18			
K769					
2450256.935	-107.14	1.49			
2450371.704	-101.88	0.94			

TABLE 4. Velocity dispersion profile

Radius (arcmin)	No Rot.	Rot.
	σ (km s ⁻¹)	σ (km s ⁻¹)
0.83	8.1 ± 1.2	7.8 ± 1.1
1.64	6.1 ± 0.9	5.8 ± 0.9
2.23	6.3 ± 1.0	6.5 ± 0.9
3.04	4.5 ± 0.7	4.5 ± 0.7
4.00	4.7 ± 0.7	4.2 ± 0.6
5.14	2.9 ± 0.4	3.0 ± 0.5
6.86	3.0 ± 0.5	2.8 ± 0.4
10.94	3.2 ± 0.5	3.3 ± 0.4

TABLE 5. Results by individual bins

Radius (arcmin)	No Rotation	Rotation			$\frac{P(\text{Rot.})}{P(\text{No Rot.})}$
	σ (km s ⁻¹)	σ (km s ⁻¹)	A (km s ⁻¹)	ϕ	
0.83	8.2 ± 1.2	7.5 ± 1.1	4.3 ± 2.1	141 ± 34	0.08
1.64	6.3 ± 0.9	5.9 ± 1.0	3.1 ± 1.9	174 ± 40	0.07
2.23	6.2 ± 1.0	6.3 ± 1.0	< 2.4	...	0.01
3.04	4.5 ± 0.7	4.4 ± 0.7	< 2.6	...	0.02
4.00	4.6 ± 0.7	3.9 ± 0.6	3.3 ± 1.2	103 ± 22	1.2
5.14	3.0 ± 0.4	3.0 ± 0.4	< 1.1	...	0.01
6.86	3.0 ± 0.5	3.0 ± 0.4	1.2 ± 0.8	106 ± 47	0.03
10.94	3.2 ± 0.4	3.3 ± 0.5	< 1.1	...	0.01
All	5.2 ± 0.3	5.1 ± 0.3	2.0 ± 0.5	131 ± 17	26.